MOX-Report No. 90/2024

Modeling anisotropy and non-stationarity through physics-informed spatial regression

Tomasetto, M.; Arnone, E.; Sangalli, L.M.

Modeling anisotropy and non-stationarity through physics-informed spatial regression

Matteo Tomasetto[1] | **Eleonora Arnone[2]** | **Laura M. Sangalli[3]**

[1]Department of Mechanical Engineering, Politecnico di Milano, Milano, Italy

[2]Department of Management, Università di Torino, Torino, Italy

[3]MOX - Department of Mathematics, Politecnico di Milano, Milano, Italy

Correspondence

Laura M. Sangalli, MOX - Department of Mathematics, Politecnico di Milano, Piazza Leonardo da Vinci, 32, 20133, Milano, Italy
Email: laura.sangalli@polimi.it

Abstract

Many spatially dependent phenomena, that are of interest in environmental problems, are characterized by strong anisotropy and non-stationarity. Moreover, the data are often observed over regions with complex conformations, such as water bodies with complicated shorelines, or regions with complex orography. Furthermore, the distribution of the data locations may be strongly inhomogeneous over space. These issues may challenge popular approaches to spatial data analysis. In this work, we show how we can accurately address these issues by spatial regression with differential regularization. We model the spatial variation by a Partial Differential Equation (PDE), defined upon the considered spatial domain. This PDE may depend upon some unknown parameters, that we estimate from the data, through an appropriate profiling estimation approach. The PDE may encode some available problem-specific information on the considered phenomenon, and permits a rich modeling of anisotropy and non-stationarity. The performances of the proposed approach are compared to competing methods, through simulation studies and real data applications. In particular, we analyse rainfall data over Switzerland, characterized by strong anisotropy, and oceanographic data in the Gulf of Mexico, characterized by non-stationarity due to the Gulf Stream.

KEYWORDS

Penalized regression, partial differential equations, parameter cascading, spatial statistics

1 | INTRODUCTION

Many spatial phenomena, that are of interest in environmental problems, are characterized by strong anisotropy and non-stationarity. For instance, winds and complicated geomorphologies may induce strong anisotropy and non-stationarity in atmospheric and meteorological data. As an example, Figure 1 illustrates daily rainfall, measured at 467 meteorological stations in Switzerland, on the 8th of May 1986 (Dubois, Malczewski, & De Cort, 2003). The data display a strongly anisotropic pattern, that likely results from the complex interaction between the geomorphology of the territory and atmospheric circulation. Similarly, water currents and complicated shorelines may induce a complex spatial distribution of data recorded in water. Furthermore, the data locations design may be strongly inhomogeneous, with the observations concentrated in a small portion of the spatial domain. Examples of these issues are given by the buoy data presented in Figure 2, top panels. The figure shows two oceanographic quantities, sea surface temperatures (top-left panel) and dissolved oxygen concentration (top-right panel), measured at moored buoys around Florida peninsula (Boyer et al., 2018; National Data Buoy Center, 2023). The collected values are strongly non-stationary, due to the presence of the *Gulf Stream*, a warm, swift and space-varying Atlantic Ocean current, which strongly influences the climate of the area. The bottom-left panel of Figure 2 displays the Gulf Stream, obtained from Earth Space Research (2009). Moreover, the morphology of the domain, with the presence of the Florida peninsula, also strongly influences the phenomenon: indeed, two oceanographic measurements observed at opposite sides of the peninsula

---

are naturally less associated than two values observed on the same side of the peninsula. In addition, the buoys are located in shallow waters, mainly near the coastlines, leaving large portions of the domain without any measurement.

The strong anisotropy and non-stationarity, the complex morphology of the spatial domain, or the highly inhomogeneous design of the observations, raise difficulties for the data analysis, that may challenge classical spatial statistics methods. In this work, we show how we can accurately address these issues, by extending a class of *Physics-Informed spatial regression models*, named *Spatial Regression with Partial Differential Equation regularisation* (SR-PDE); see, e.g., Sangalli (2021). In particular, we model the space variation by a Partial Differential Equation (PDE), defined over the spatial domain of interest. With respect to previous works on SR-PDE, we here consider PDEs that may depend upon some unknown parameters, and we propose an appropriate profiling estimation approach to estimate such parameters. This enable us, in one hand, to encode problem-specific information on the considered phenomenon, whenever some (partial) knowledge of the phenomenon is available; in the other hand, it permits a very rich modeling of anisotropy and non-stationarity.

The use of deterministic and stochastic differential equations, in spatial statistics models, has been explored since the pioneering work of Whittle (1954), for different purposes: enabling faster computations, permitting a flexible modeling of the space and space-time variation, and leveraging on mechanistic information about the phenomenon at hand. In particular, the inclusion of problem-specific differential equations in spatial statistics methods has been popularized by Berliner (2003). Examples in this direction are offered, e.g., by Wikle (2003), Wikle and Hooten (2010), Cressie and Wikle (2011), Kuhnert (2014), Richardson (2017) and Hefley, Hooten, Russell, Walsh, and Powell (2017), where mechanistic information is used to inform dynamical spatio-temporal models. Peli, Menafoglio, Cervino, Dovera, and Secchi (2022) propose instead a Physics-based Residual Kriging, that incorporates a physical model, expressed by a PDE, in a universal kriging setting. On a different modeling framework, Lindgren, Rue, and Lindström (2011), Bolin and Lindgren (2011) and Cameletti, Lindgren, Simpson, and Rue (2013) describe complex spatial behaviours by a stochastic PDE (sPDE), properly fitted through Integrated Nested Laplace Approximation (INLA, see Rue, Martino, & Chopin, 2009). See Krainski et al. (2018) and Lindgren, Bolin, and Rue (2022) for a complete overview of the sPDE approach, with possible extensions and applications. In this framework, the possibly non-trivial shape of the domain can be accounted for the so-called barrier model, proposed in Bakka, Vanhatalo, Illian, Simpson, and Rue (2019). In addition, Fuglstad, Lindgren, Simpson, and Rue (2015), Fuglstad, Simpson, Lindgren, and Rue (2015) and Chaudhuri, Juan, Saurina, Varga, and Saez (2023) explain how to face non-stationarity in this context.

Other fascinating research directions move towards the use of deep learning approaches. Indeed, some recent proposals, to enable a very flexible modeling of spatial variation, rely on neural networks. For example, the DeepKriging model by Chen, Li, Reich, and Sun (2022) takes into account deep neural networks to better capture the spatial dependence among data. Deep learning techniques are also considered by Zammit-Mangion and Wikle (2020), to model the space-time varying dynamics in a highly flexible way. Lenzi, Bessac, Rudi, and Stein (2023) considers neural networks to estimate unknown parameters in the context of spatial intractable models. See Wikle and Zammit-Mangion (2023) for a recent review. In this framework, Physics-Informed deep learning approaches to spatial data analysis are now being explored, by, e.g., Bonas and Castruccio (2023), Bonas, Richter, and Castruccio (2023) and Menicali, Richter, and Castruccio (2023), leveraging on the separate literature on Physics-Informed Neural Networks, that currently constitutes a cutting-edge research direction in deep learning.

Partial differential operators and PDEs are also employed in regularizing terms of nonparametric regression models used for spatial data analysis problems. The classical models in this framework, such as tensor product splines or thin-plate splines (Cox, 1984; Eubank, 1999; Wahba, 1981, 1990), include simple isotropic differential operators in the penalty term. Extensions accounting for the shape of the spatial domain are considered for instance by T. Ramsay (2002), who introduce FELsplines, Wood, Bravington, and Hedley (2008), Marra, Miller, and Zanin (2012) and Augustin, Trenkel, Wood, and Lorance (2013), who present the so-called soap film smoothing, H. Wang and Ranalli (2007), Scott-Hayward, Mackenzie, Donovan, Walker, and Ashe (2014), who propose low-rank thin-plate spline approximations, and Lai and Schumaker (2007), Lai and Wang (2013), who use bivariate splines over triangulations (see, e.g., the review in L. Wang, Wang, Lai, & Gao, 2020; Yu, Wang, Wang, Liu, & Yang, 2019). The same family of methods embraces as well the above mentioned Spatial Regression with Partial Differential Equation regularisation, originally introduced in Sangalli, Ramsay, and Ramsay (2013), Azzimonti, Nobile, Sangalli, and Secchi (2014) and Azzimonti, Sangalli, Secchi, Domanin, and Nobile (2015) as a generalization of the proposed by T. Ramsay (2002). SR-PDE can handle multidimensional spatial domains with complex shapes, including general two-dimensional curved domains (Ettinger, Perotto, & Sangalli, 2016) and non-convex three-dimensional domains (Arnone, Negri, Panzica, & Sangalli, 2023). The regularizing term of SR-PDE may involve general forms of linear second-order PDEs, that encode the available physical knowledge of the phenomenon under study (Arnone, Azzimonti, Nobile, & Sangalli, 2019; Azzimonti et al., 2014, 2015).
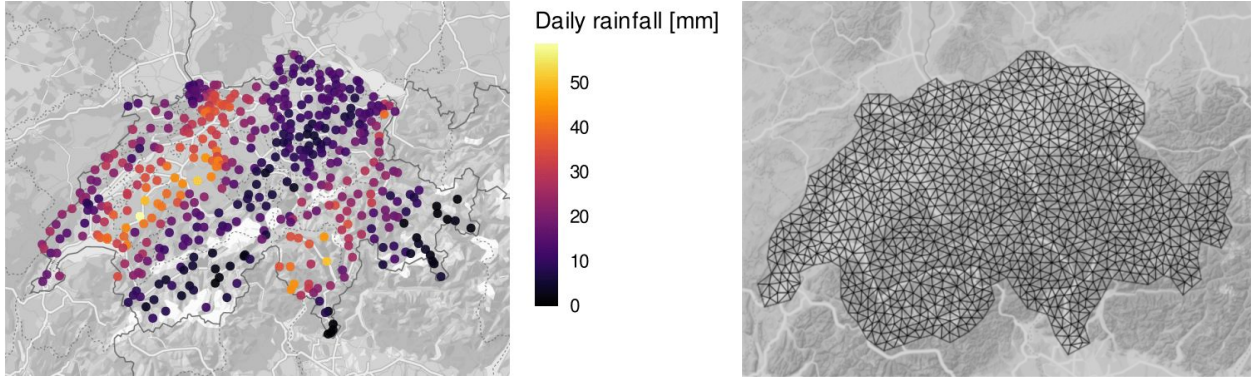
FIGURE 1 Switzerland rainfall data. Left: daily rainfall measurements, recorded at 467 locations on the Swiss territory, on May 8, 1986. Right: regular mesh of the Swiss territory.

Outside of the simple isotropic and stationary case, SR-PDE approaches, so far presented in the literature, usually require that the PDE in the regularizing term is fully specified by the modeler. However, in typical applications, the problem-specific information may be unavailable, incomplete or inaccurate. For instance, in the application to rainfall measurements over Switzerland, we can appreciate a clear anisotropic pattern in the data, likely due to the interaction between atmospheric circulation and geomorphology, but we lack a PDE description of this phenomenon. In the application to buoy data, we only have a partial information, concerning the presence of the Gulf Stream, that can be encoded in the transport term of a linear second-order PDE; however, we miss the full specification of the governing PDE. In all these cases, it is impossible to fix all the parameters in the regularizing PDE, on the basis of the problem-specific information.

In the present work, differently from standard SR-PDE approaches, we consider the challenging situation where the PDE in the regularizing term of a SR-PDE model is only specified up to unknown parameters. Considering PDEs with unknown parameters enable us to fully deploy the modeling potential of PDEs, one of the most powerful mathematical tools to model complex phenomena behaviors. Moreover, it allows us to naturally describe strong forms of anisotropy and non-stationarity, over spatial domains with complex conformations. We devise an appropriate profiling estimation technique, to accurately estimate, within the considered spatial data analysis problem, the unknown stationary parameters that specify the (possibly non-stationary) PDE terms. This profiling estimation technique is based on the so-called *parameter cascading* approach. Parameter cascading was originally introduced by J. O. Ramsay, Hooker, Campbell, and Cao (2007) in order to estimate the parameters of an ordinary differential equation, starting from noisy measurements of its solution, and later extended by Xun, Cao, Mallick, Maity, and Carroll (2013) to approximate PDE parameters. A first exploration of the parameter cascading approach, in the context of SR-PDE, was done in Bernardi, Carey, Ramsay, and Sangalli (2018), focusing on the special case when the penalty involves only a stationary anisotropic diffusion term, on a two-dimensional domain. In this paper, we extend this approach to deal with the more general case where the penalty involves general linear second-order elliptic PDEs, with space-varying differential operators, and where all the (possibly non-stationary) PDE terms may depend upon unknown stationary parameters; we moreover consider both two-dimensional and three-dimensional domains. The proposed approach highly enhances the scope and the modeling flexibility of this class of Physics-Informed regression models. The implementation of the proposed method is based on the R package `fdaPDE` available from `CRAN` (Arnone et al., 2024).

The paper is organized as follows. Section 2 reviews the SR-PDE modeling framework, when the PDE is fully specified a priori. Section 3 proposes a strategy to estimate the PDE parameters, when the underlying physics is missing or incomplete. Section 4 shows the performances of the proposed approach in some simulation studies. Section 5 and Section 6 illustrate the use of the proposed method in real case studies characterized by anisotropy and non-stationarity. In particular, Section 5 describes the application to rainfall data, whilst Section 6 presents the application to buoy data. Section 7 discusses ideas about possible extensions of the proposed approach.
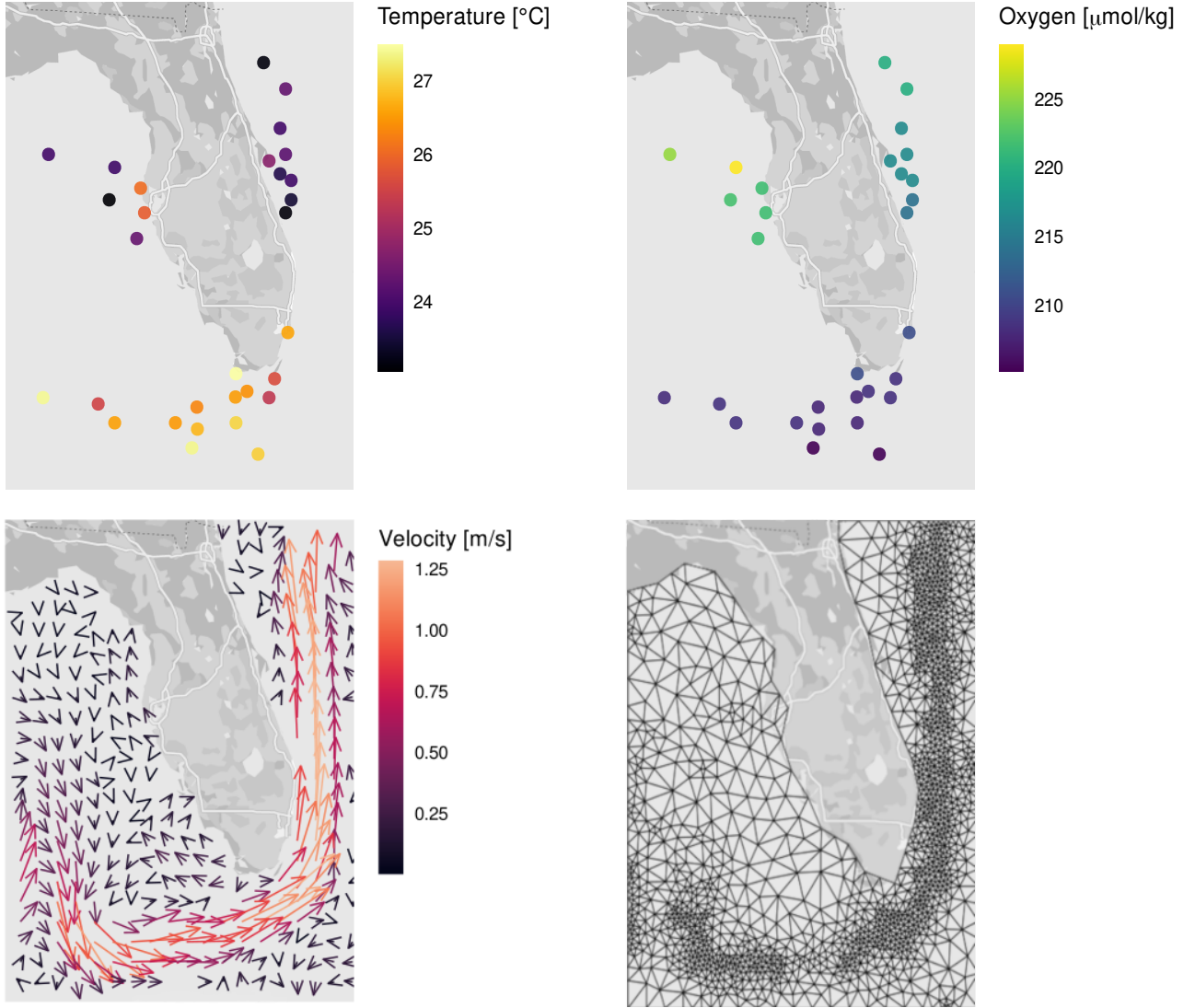
FIGURE 2 Buoy data around Florida peninsula. Top: sea surface temperature (left) and dissolved oxygen concentration (right) measured at moored buoys placed around the Florida coastlines. Bottom left: Gulf Stream velocity around Florida peninsula. Bottom right: data-driven mesh generated by refining a coarser regular mesh where the Gulf Stream displays high velocity.

2 | SPATIAL REGRESSION WITH PDE REGULARISATION

This section reviews Spatial Regression with PDE regularisation (SR-PDE), presenting the solution to the estimation problem when the PDE in the regularising term is fully specified. For simplicity of exposition we focus on spatial data, and only briefly comment on possible generalizations to space-time data in the final discussion section.

2.1 | Modeling formulation

Consider a d-dimensional domain $\mathcal{D} \subset \mathbb{R}^d$ with $d = 2, 3$. The domain $\mathcal{D}$ can be a non-convex 2D or 3D region, or a 2D Riemannian manifold, i.e., a curved surface. The irregular shape of the domain may for instance result from geographic constraints or complicated conformations, such as coastal regions with irregular shorelines, as in the application to buoy data in Figure 2, or curved regions with complex orography. Denote by $\mathbf{p}_i \in \mathcal{D}$, for $i = 1, ..., n$, the n locations inside the domain $\mathcal{D}$, where the

data are recorded. Let y_i be the real-valued responses, observed at the locations $\mathbf{p}_i$, and $\mathbf{x}_i = (x_{i,1}, \ldots, x_{i,q})^\top$ the q-dimensional vectors containing the covariates associated with y_i and measured at $\mathbf{p}_i$. Assume the semiparametric model

$$\mathbf{y} = X\boldsymbol{\beta} + \mathbf{f}_n + \boldsymbol{\varepsilon}$$

where $\mathbf{y} = (y_1, ..., y_n)^\top$ is the vector of responses, $X = (\mathbf{x}_1, ..., \mathbf{x}_n)^\top$ is the $n \times q$ regressor matrix, $\boldsymbol{\beta} \in \mathbb{R}^q$ is the vector of coefficients accounting for the mean effect of the covariates, $\mathbf{f}_n = (f(\mathbf{p}_1), ..., f(\mathbf{p}_n))^\top$ is the vector collecting the evaluations of the unknown spatial function $f : \mathcal{D} \to \mathbb{R}$ at the n data locations, and $\boldsymbol{\varepsilon} = (\varepsilon_1, ..., \varepsilon_n)^\top$ is the vector of independent and identically distributed measurements errors, having zero mean and finite variance σ^2. Moreover, let $L_\mathcal{D}f = u$ be a PDE, that provides a partial description of some known characteristics of the underlying spatial function f, as detailed in Section 2.2. In SR-PDE, the two unknowns, $\boldsymbol{\beta}$ and f, are estimated by minimizing the following penalized residual sum of squares:

$$J_\rho(\boldsymbol{\beta}, f) = (1-\rho)\frac{1}{n}\sum_{i=1}^{n}\left(y_i - \mathbf{x}_i^\top\boldsymbol{\beta} - f(\mathbf{p}_i)\right)^2 + \rho\frac{1}{|\mathcal{D}|}\int_\mathcal{D}(L_\mathcal{D}f - u)^2\,d\mathbf{p} \quad \text{for } \rho \in (0, 1) \tag{1}$$

where ρ is the smoothing parameter that governs the balance between data fitting and model fidelity, and $|\mathcal{D}| = \int_\mathcal{D} d\mathbf{p}$ is the area or volume of the domain $\mathcal{D}$. The estimation functional (1) includes, in addition to the usual residual sum of squares, also a penalization term that involves the squared misfit over $\mathcal{D}$ of the PDE $L_\mathcal{D}f = u$. Through this extra information, the model can embed complex physics-based information, concerning the spatial structure of the phenomenon being analysed, as well as the shape of spatial domain $\mathcal{D}$.

2.2 | Regularizing PDE

SR-PDE is currently implemented for linear second-order elliptic PDEs $L_\mathcal{D}f = u$, with diffusion-transport-reaction operators of the form

$$L_\mathcal{D}f = -\nabla \cdot (K\nabla f) + \mathbf{b} \cdot \nabla f + cf$$

where ∇ is defined as $\left(\frac{\partial}{\partial p_1}, \frac{\partial}{\partial p_2}\right)^\top$ if $d = 2$, and $\left(\frac{\partial}{\partial p_1}, \frac{\partial}{\partial p_2}, \frac{\partial}{\partial p_3}\right)^\top$ if $d = 3$, while p_ℓ, for $\ell = 1, ..., d$, denotes the coordinates of the reference system. The parameters K, $\mathbf{b}$, c and u may vary over space, and are named, respectively, Diffusion, Transport, Reaction and Forcing term. Such names refer to the role that these different terms have in time-dependent problems, but that result in effects that are also appreciable at fixed time, as detailed below.

Diffusion term. The diffusion term is defined as $\nabla \cdot (K\nabla f) = \sum_{\ell=1}^{d}\frac{\partial}{\partial p_\ell}\left(\sum_{s=1}^{d}K_{\ell,s}\frac{\partial f}{\partial p_s}\right)$, where $K = \{K_{\ell,s}\}$, for $\ell, s = 1, ..., d$, is a $d \times d$ symmetric and positive definite tensor. This term models anisotropy. The first two columns of Figure 3 visualize the effects of this term on a 2D domain, through ellipsoids having the axes oriented as the eigenvectors of K, and lengths proportional to the corresponding eigenvalues. The first column concerns the special case when $K = \eta I$, where I is the identity matrix and η is a real coefficient. In this case, the diffusion term induces an isotropic effect. This effect may have the same intensity across the whole domain, when η is constant over space (stationary isotropy, in the top-left panel), or may have a space-varying intensity, as modeled by $\eta(\mathbf{p})$ (non-stationary isotropy, in the bottom-left panel). The second column in Figure 3 displays instead examples of anisotropic patterns, when $K \neq \eta I$. Also in this case, the anisotropy may have constant orientation and intensity, when K is constant in space (stationary anisotropy, in the top-center panel), or vary over space, considering a function of space $K(\mathbf{p})$ (non-stationary anisotropy, bottom-center panel). For instance, regarding the application to rainfall data on the Swiss territory, detailed in Section 5, we use the tensor K to model the range and the preferential direction of a stationary anisotropy.

Transport term. The transport term $\mathbf{b} \cdot \nabla f = \sum_{\ell=1}^{d}b_\ell\frac{\partial f}{\partial p_\ell}$, where $\mathbf{b}$ is a d-dimensional vector, steers direction and intensity of a one-directional effect. The third column in Figure 3 visualizes the effect of the transport term. The transport may have constant direction and intensity over the domain (stationary transport, in the top-right panel), or space-varying direction and/or intensity, modeled by the function $\mathbf{b}(\mathbf{p})$ (non-stationary transport, in the bottom-right panel). For example, in the application to Switzerland rainfall data, in Section 5, we consider a stationary transport term $\mathbf{b}$ to model a prevailing wind. Instead, in the application to buoy data, in Section 6, we consider the non-stationary transport term $\mathbf{b}(\mathbf{p})$ illustrated in the bottom-left panel of Figure 3, to model the Gulf Stream around Florida peninsula.
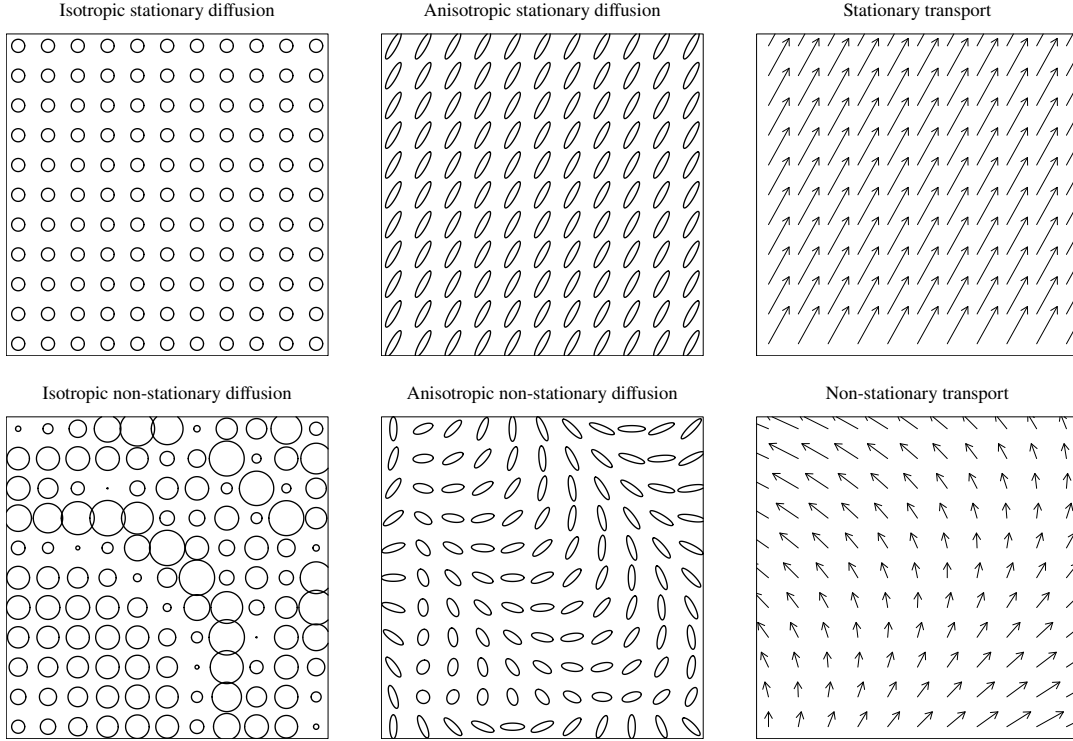
FIGURE 3 Visualization of possible spatial patterns induced by different PDE terms. Top left: isotropic stationary diffusion, obtained for $K = \eta I$ with η constant in space. Bottom left: isotropic non-stationary diffusion, obtained for $K = \eta I$ considering $\eta(\mathbf{p})$ as a function of space. Top center: anisotropic stationary diffusion, obtained for $K \neq \eta I$ with K constant in space. Bottom center: anisotropic non-stationary diffusion, obtained for $K \neq \eta I$ considering $K(\mathbf{p})$ as a function of space. Top right: stationary transport, obtained for $\mathbf{b}$ constant in space. Bottom right: non-stationary transport, obtained considering $\mathbf{b}(\mathbf{p})$ as a function of space.

Reaction term. The reaction term cf, where c is a real-valued coefficient, controls shrinking of the solution towards the zero function. Also this term may vary over space.

Forcing term. The forcing term $u \in L^2(\mathcal{D})$, in the PDE $L_{\mathcal{D}}f = u$, can be used to model sources in the signal under study. For instance, in the analysis of wildfire propagation (see, e.g., Grieshop & Wikle, 2023), a non-homogeneous forcing term $u(\mathbf{p})$ could be used to model the spatial distribution of sources of fire, such as tanks of fuel, or other deposits of inflammable materials, over the considered spatial domain. For simplicity of exposition, in this work we consider homogeneous forcing terms $u = 0$, and refer the readers to, e.g., Azzimonti et al. (2014, 2015) for details on the non-homogeneous case.

Boundary conditions. It is also possible to specify different case-specific conditions on the boundary $\partial \mathcal{D}$. These conditions may concern the values of the function f, or of its normal derivatives, and may vary over different portions of the domain. For simplicity of exposition, in the following sections we consider homogeneous Neumann conditions (i.e., null normal derivative of f on $\partial \mathcal{D}$). These boundary conditions, also known as natural conditions, are not strictly imposed in the estimation problem, and the resulting estimate satisfies them only approximately. We refer the readers to, e.g., Azzimonti et al. (2014, 2015) for details on how to handle different boundary conditions.

We use the notation SR-PDE$(K, \mathbf{b}, c)$ to indicate a SR-PDE model with PDE terms K, $\mathbf{b}$ and c. The simplest setting for SR-PDE is the fully stationary isotropic case, obtained for $K = I$, $\mathbf{b} = \mathbf{0}$, $c = 0$, $u = 0$, and homogeneous Neumann boundary conditions, and we refer to this model as SR-PDE$(I, \mathbf{0}, 0)$. This corresponds to penalization of the simple Laplace operator

$$\Delta f = \nabla \cdot \nabla f = \sum_{\ell=1}^{d} \frac{\partial^2 f}{\partial p_\ell^2}$$

that measures the local curvature of the spatial function f along every direction in the same way. This special case is the default choice in absence of any problem-specific information, or any apparent anisotropic behaviour in the data.

With the exception of Bernardi et al. (2018), the literature on SR-PDE has so far focused on isotropic and stationary models, alike SR-PDE$(I, \mathbf{0}, 0)$, or else on cases where the PDE terms K, $\mathbf{b}$ and c were fully specified on the basis of problem-specific knowledge (see, e.g., Arnone et al., 2019; Azzimonti et al., 2014, 2015). Section 2.3 briefly reviews the solution for the SR-PDE estimation problem when the underlying physics is fully specified.

2.3 | Solution to the estimation problem when the underlying physics is fully specified

Azzimonti et al. (2014, 2015) and Arnone, Negri, et al. (2023) show that, for given K, $\mathbf{b}$ and c, i.e., when the underlying physics is fully specified, the estimation problem is well-posed for $\boldsymbol{\beta} \in \mathbb{R}^q$ and f in a general space of functions with appropriate regularity. However, such estimation problem is infinite-dimensional and does not possess a closed form solution. Therefore, numerical analysis techniques, such as the Finite Element Method (FEM), are required to discretize the problem and obtain a solution. The general idea of FEM is to partition the spatial domain $\mathcal{D}$ into a set of subdomains: these subdomains can be triangles in 2D or tetrahedra in 3D. For instance, the right panel of Figure 1 shows a regular triangulation of the Swiss territory, used for the application to rainfall data, detailed in Section 5. The bottom-right panel of Figure 2 shows instead a data-driven mesh for the application to buoy data, discussed in Section 6.

Based on the considered mesh, it is then possible to define a set of finite element bases, that are locally-supported piecewise polynomial functions. Such system of bases spans the space of globally continuous functions over the mesh, that are polynomials of the desired order when restricted to an element of the mesh. The function f is thus represented by an extension in such bases, so that, instead of searching for f in an infinite-dimensional space of functions, it is enough to look for the coefficients $\mathbf{f}$ of its basis expansion. Let Ψ be the matrix whose columns store the evaluations of every finite element basis at the locations $\mathbf{p}_1, ..., \mathbf{p}_n$. Define the residualizing matrices

$$Q = I - X(X^\top X)^{-1} X^\top$$
$$\Lambda = I - \Psi \left(\frac{1-\rho}{n} \Psi^\top \Psi + \frac{\rho}{|\mathcal{D}|} P \right)^{-1} \frac{1-\rho}{n} \Psi^\top$$

where P is the matrix denoting the finite element discretization of the penalization term; see Section 7.1 of the Supporting Information for details. The solution to the discretized estimation problem is then given by

$$\hat{\boldsymbol{\beta}} = \left(X^\top \Lambda X \right)^{-1} X^\top \Lambda \mathbf{y}$$
$$\hat{\mathbf{f}} = \left(\frac{1-\rho}{n} \Psi^\top Q \Psi + \frac{\rho}{|\mathcal{D}|} P \right)^{-1} \frac{1-\rho}{n} \Psi^\top Q \mathbf{y}. \tag{2}$$

Note that the expressions of the estimators in Equation (2) depend implicitly on the PDE parameters, through the penalty matrix P. Therefore, the estimate depends on the physical model. In particular, Section 7.2 of the Supporting Information shows how the first and second order properties of the estimators $\hat{\boldsymbol{\beta}}$ and $\hat{f}$ depends on the penalty matrix P. Additionally, asymptotic Gaussianity of the estimators, shown, e.g., in Arnone, Negri, et al. (2023); Ferraccioli, Sangalli, and Finos (2022, 2023), justifies Wald-type inference, as detailed in the former works. More advanced inferential tools, based on innovative resampling strategies, are discussed in Cavazzutti et al. (2024); Ferraccioli et al. (2022, 2023).

3 | SOLUTION TO THE ESTIMATION PROBLEM WHEN THE UNDERLYING PHYSICS IS MISSING OR INCOMPLETE

In most analyses of spatially distributed data, our problem-specific information on the process driving the phenomenon being analysed is incomplete or imperfect. For instance, in the application to Switzerland rainfall data, detailed in Section 5, we lack a PDE description of the rainfall phenomenon. However, the data display a clear anisotropic pattern, calling for a diffusion term with unknown stationary matrix $K \neq \eta I$. Moreover, we might expect that the rainfall on May 8, 1986, was accompanied by wind, which we could model through a transport term. Unfortunately, no information is available on the wind on the day of these records. We can though model the unknown prevailing wind on the day of the records by a transport term, with an

unknown stationary vector **b**. Regarding the application to buoy data, discussed in Section 6, the physics is partially available. Indeed, we know about the presence of the Gulf Stream, illustrated in the bottom-left panel of Figure 2, and this information can be properly encoded in the non-stationary transport term. However, we do not know a priori how to appropriately balance this transport term with a diffusion term, so we need to estimate the stationary intensity η of an isotropic diffusion matrix $K = \eta I$. In these settings, the PDE can only be specified up to some unknown stationary parameters, that define the (possibly non-stationary) PDE terms. Hence from a modeling perspective, in the SR-PDE framework it is crucial to define appropriate estimation approaches to estimate these unknown parameters from data, jointly with the vector of parameters β and the function f. To this aim, we here develop an appropriate estimation procedure, that follows the parameter cascading approach.

3.1 | A parameter cascading approach for SR-PDE with unknown PDE parameters

Our new objective functional $J_\rho(\beta, f; K, \mathbf{b}, c)$ is defined as in Equation (1), but we now consider as unknowns also the PDE terms K, **b** and c, or a subset of these parameters. Specifically, the (possibly non-stationary) PDE terms may depend on multiple unknown stationary parameters, along with the parametrization of the PDE terms detailed in Section 3.2. The objective functional $J_\rho(\beta, f; K, \mathbf{b}, c)$ is not convex in all the unknowns; thus it is impossible to minimize it jointly in all the unknowns. Therefore, an iterative multi-step algorithm is required to solve the estimation problem. We here propose an iterative procedure based on a parameter cascading approach. To this end, we also consider the Sum of Squared Error (SSE),

$$SSE(\hat{\beta}, \hat{f}; \hat{K}, \hat{\mathbf{b}}, \hat{c}) = \sum_{i=1}^{n} (y_i - \mathbf{x}_i^\top \hat{\beta} - \hat{f}(\mathbf{p}_i))^2.$$

The SSE depends on the PDE parameters $\hat{K}$, $\hat{\mathbf{b}}$ and $\hat{c}$ only implicitly, through the estimators $\hat{\beta}$ and $\hat{f}$, as described by Equation (2). The iterative optimization scheme works as follows. Let $\hat{\beta}_j, \hat{f}_j, \hat{K}_j, \hat{\mathbf{b}}_j$ and $\hat{c}_j$ be the estimates after j iterations; at iteration $j + 1$ the algorithm performs the following steps:

1. Given $\hat{K}_j, \hat{\mathbf{b}}_j, \hat{c}_j$, the estimate $\hat{\beta}_{j+1}$ and $\hat{f}_{j+1}$ that solve

$$\left\{ \hat{\beta}_{j+1}, \hat{f}_{j+1} \right\} = \underset{\beta, f}{\operatorname{argmin}} \, J_\rho \left(\beta, f; \hat{K}_j, \hat{\mathbf{b}}_j, \hat{c}_j \right).$$

   are obtained using the formulas in Equation (2).
2. Given $\hat{\beta}_{j+1}, \hat{f}_{j+1}$ computed in the previous step, the estimate $\hat{K}_{j+1}, \hat{\mathbf{b}}_{j+1}$ and $\hat{c}_{j+1}$, in cascade, are obtained solving

$$2.1. \quad \hat{K}_{j+1} = \underset{K}{\operatorname{argmin}} \, SSE(\hat{\beta}_{j+1}, \hat{f}_{j+1}; K, \hat{\mathbf{b}}_j, \hat{c}_j),$$

$$2.2. \quad \hat{b}_{j+1} = \underset{\mathbf{b}}{\operatorname{argmin}} \, SSE(\hat{\beta}_{j+1}, \hat{f}_{j+1}; \hat{K}_{j+1}, \mathbf{b}, \hat{c}_j),$$

$$2.3. \quad \hat{c}_{j+1} = \underset{c}{\operatorname{argmin}} \, SSE(\hat{\beta}_{j+1}, \hat{f}_{j+1}; \hat{K}_{j+1}, \hat{\mathbf{b}}_{j+1}, c).$$

Solution to Step 1 is equivalent to the estimation problem with known PDE terms, discussed in Section 2.3; this step does not require any iterative optimization, as the corresponding estimators are provided in Equation (2). Step 2 defines instead three new complex minimization problems to be performed. Since the SSE depends on the PDE parameters only implicitly, through the values of $\hat{\beta}_{j+1}$ and $\hat{f}_{j+1}$ computed in Step 1, the estimation problems in Steps 2.1, 2.2 and 2.3 require a numerical optimization method, such as, e.g., Gradient Descent, Conjugate Gradient method, BFGS, L-BFGS-B or Nelder-Mead method. The initial values K_0, $\mathbf{b}_0$ and c_0 are set respectively to $I, \mathbf{0}, 0$, unless a more informative problem-specific knowledge is available.

It is important to notice that it is not necessary to estimate all the PDE terms. Indeed, thanks to the sequential nature of the cascade, there is complete freedom to choose the terms to be estimated, among K, **b** and c, and all the combinations are possible. For instance, in the application to rainfall data in Section 5, we estimate the diffusion matrix K, to model the apparent anisotropy in the data, and the transport vector **b**, to include a possible transport effect induced by wind, with unknown direction and intensity, since we lack information about the wind on the day of the records; the reaction terms is set to zero since it does not appear relevant for the problem under study. In the application to buoy data in Section 6, we estimate the diffusion parameter K, while we fix the transport term, that encodes the Gulf Stream, and is thus specified on the basis of problem-specific knowledge;

also in this case, the reaction is set to zero, since it is irrelevant for the problem under study. It should also be pointed out that it may be that only some of the coefficients in the terms K, $\mathbf{b}$ and c are unknown. The estimate is thus typically limited to only a few parameters of these terms. For example in the application to buoy data, we only estimate the intensity η of the diffusion term. Finally, the cascade order in the algorithm, $K \to \mathbf{b} \to c$, is here considered because the estimate of K is less sensitive to the specific values of the other PDE terms, compared to $\mathbf{b}$ and c.

3.1.1 | Selection of the smoothing parameter

The smoothing parameter ρ, in the estimation functional in Equation (1), governs the balance between fidelity to the empirical model, as encoded by the SSE term, and fidelity to the physical model, as encoded by the regularizing PDE. This smoothing parameter must be properly chosen to ensure accurate results. In the context of SR-PDE, the selection of ρ is performed through minimization of the Generalized Cross Validation index (GCV) (Craven & Wahba, 1978), given by

$$\text{GCV}(\rho; K, \mathbf{b}, c) = \frac{n}{(n - q - \text{tr}(S))^2} \left(\mathbf{y} - \hat{\mathbf{y}}\right)^\top \left(\mathbf{y} - \hat{\mathbf{y}}\right) = \frac{n}{(n - q - \text{tr}(S))^2} \, SSE(\hat{\boldsymbol{\beta}}, \hat{f}; \hat{K}, \hat{\mathbf{b}}, \hat{c}),$$

where S is the smoothing matrix defined as

$$S = \Psi \left(\frac{1 - \rho}{n} \Psi^\top Q \Psi + \frac{\rho}{|\mathcal{D}|} P \right)^{-1} \frac{1 - \rho}{n} \Psi^\top Q$$

$tr(S)$ denotes its trace. Notice that the GCV depends implicitly on the smoothing parameter ρ and on the PDE terms, through S and $\hat{\mathbf{y}}$.

However, simulations studies highlights that the parameter cascading procedure requires very different smoothing parameters, in the Steps 1 and 2, to achieve optimal results. Similar considerations were noted by Bernardi et al. (2018), which explored parameter cascading in the simpler setting where only a stationary anisotropic diffusion term is considered (with null transport and reaction), on 2D domains. Indeed, in Step 1, small values of ρ are usually optimal to appropriately balance fidelity to the data, measured by the SSE, and fidelity to the physical model, encoded by the regularizing PDE. Instead, when estimating the PDE parameters, in Step 2, larger values of ρ are needed to emphasize the effect of the PDE. To take into account this issue, the parameter cascading procedure is organized as detailed in Algorithm 1. Specifically, the PDE parameters are estimated for different smoothing parameters, in a grid of values $\{\rho_1, ..., \rho_M\}$, spanning the whole interval $(0, 1)$. Among the M candidate estimates of the PDE parameters, obtained in correspondence of the M different smoothing parameter values, $\{\rho_1, ..., \rho_M\}$, we select the estimates providing the lowest GCV. Moreover, in order to gain flexibility, we find the initial estimates of K, $\mathbf{b}$, and c sequentially, thus allowing for different optimal ρ values. As detailed in Algorithm 1, when more than one PDE term is unknown, the estimation of the PDE parameters is repeated iteratively, until a suitable convergence criterion is met. This allows us to refine the results, while avoiding suboptimal solutions, that may dependent on the chosen cascade order. It is important to notice that the exploration of the grid of the smoothing parameter values, $\{\rho_1, ..., \rho_M\}$, is required only once. Indeed, as verified in simulations, subsequent iterations always select the same optimal smoothing parameters, ρ_K, $\rho_\mathbf{b}$ and ρ_c, that are found in the first optimization. In addition, the algorithm is amenable to parallelization, to speed up the entire procedure.

3.2 | Parametrization of diffusion and transport terms

This section describes in detail the parametrization of the diffusion matrix and transport vector. The reader not interested to these technical aspects, may skip this section.

3.2.1 | 2D parametrization of diffusion and transport

In spatial data analysis problems over 2D domains, two parameters are required to parametrize the diffusion K:

- $\alpha \in [0, \pi]$: the angle indicating the direction of anisotropy. In the visualization of Figure 3, this parameter specifies the main direction of anisotropy, identifying the orientation of the ellipse associated with K. The angle α is taken in the interval $[0, \pi]$ since, in the considered parametrization, K is π-periodic with respect to this quantity.

Algorithm 1 Iterative parameter cascading

```
▷ First diffusion estimation
for m = 1,...,M, do
    Given ρ = ρ_m,  b = b_0,  c = c_0,  find K̂^(m) via Step 1 and Step 2.1
end for
Find m* = argmin GCV(ρ; K^(m), b_0, c_0) and set K̂ = K̂^(m*),  ρ_K = ρ_{m*}
         1,...,m

▷ First transport estimation
for m = 1,...,M, do
    Given ρ = ρ_m,  K = K̂,  c = c_0,  find b̂^(m) via Step 1 and Step 2.2
end for
Find m* = argmin GCV(ρ; K̂, b^(m), c_0) and set b̂ = b̂^(m*),  ρ_b = ρ_{m*}
         1,...,m

▷ First reaction estimation
for m = 1,...,M, do
    Given ρ = ρ_m,  K = K̂,  b = b̂,  find ĉ^(m) via Step 1 and Step 2.3
end for
Find m* = argmin GCV(ρ; K̂, b̂, c^(m)) and set ĉ = ĉ^(m*),  ρ_c = ρ_{m*}
         1,...,m

▷ Iterative refinement
while !convergence do
    Given ρ = ρ_K,  b = b̂,  c = ĉ,  find K̂ via Step 1 and Step 2.1
    Given ρ = ρ_b,  K = K̂,  c = ĉ,  find b̂ via Step 1 and Step 2.2
    Given ρ = ρ_c,  K = K̂,  b = b̂,  find ĉ via Step 1 and Step 2.3
end while
```

- $\gamma \in (1, +\infty)$: the ratio between the maximum and the minimum eigenvalue of K. This parameter represents the intensity of anisotropy: the farther away from 1, the more elongated is the ellipse representing the anisotropic effect modeled by K.

The diffusion tensor K is then parametrized as

$$K(\alpha, \gamma) = R(\alpha)\Sigma(\gamma)R(\alpha)^{-1}$$

where

$$R(\alpha) = \begin{bmatrix} \cos(\alpha) & -\sin(\alpha) \\ \sin(\alpha) & \cos(\alpha) \end{bmatrix} \quad \text{and} \quad \Sigma(\gamma) = \begin{bmatrix} \frac{1}{\sqrt{\gamma}} & 0 \\ 0 & \sqrt{\gamma} \end{bmatrix}.$$

Notice that $R^{-1} = R^\top$ since R is a rotation matrix. When the diffusion is considered along with transport or reaction, a multiplicative coefficient η is introduced, to model the intensity of the diffusion term, and its relative magnitude with respect to the transport and/or reaction term. If b and c are both null, the parameter η is unnecessary, since the intensity of the diffusion term is modeled directly by the smoothing parameter ρ, which is estimated minimizing the GCV index.

To parametrize the transport vector b over 2D domains, we use polar coordinates, i.e.,

$$\mathbf{b}(\varphi, r) = (r\cos(\varphi), r\sin(\varphi))^\top$$

where $\varphi \in [0, 2\pi]$ is the angle indicating the direction of the transport vector, and $r \in [0, +\infty)$ represents its module.

3.2.2 | 3D parametrization for diffusion and transport

In spatial data analysis problems over in 3D domains, four parameters are required to parametrize the diffusion K:

- $\alpha_1 \in [0, 2\pi]$: the first anisotropy angle; this parameter specifies the counterclockwise rotation angle of the ellipsoid with respect to the p_3-axis.
- $\alpha_2 \in [0, 2\pi]$: the second anisotropy angle; this parameter specifies the counterclockwise rotation angle of the ellipsoid with respect to the p_2-axis.
- $\gamma_1 \in (1, +\infty)$: the ratio between the largest and the smallest eigenvalue of K; this parameter relates to the intensity of the anisotropy, setting the range in the direction associated with the maximum eigenvalue of K with respect to that associated with the minimum eigenvalue of K.
- $\gamma_2 \in (1, +\infty)$: the ratio between the middle and the smallest eigenvalue of K; this parameter can be interpreted analogously as γ_1. Notice that $\gamma_2 \leq \gamma_1$ by definition.

The diffusion tensor K is then parametrized as

$$K(\alpha_1, \alpha_2, \gamma_1, \gamma_2) = R(\alpha_1, \alpha_2)\Sigma(\gamma_1, \gamma_2)R(\alpha_1, \alpha_2)^{-1}$$

where

$$R(\alpha_1, \alpha_2) = \begin{bmatrix} \cos(\alpha_1) & -\sin(\alpha_1) & 0 \\ \sin(\alpha_1) & \cos(\alpha_1) & 0 \\ 0 & 0 & 1 \end{bmatrix} \cdot \begin{bmatrix} \cos(\alpha_2) & 0 & \sin(\alpha_2) \\ 0 & 1 & 0 \\ -\sin(\alpha_2) & 0 & \cos(\alpha_2) \end{bmatrix} \quad \text{and} \quad \Sigma(\gamma_1, \gamma_2) = \begin{bmatrix} \sqrt[3]{\frac{\gamma_1^2}{\gamma_2}} & 0 & 0 \\ 0 & \sqrt[3]{\frac{\gamma_2^2}{\gamma_1}} & 0 \\ 0 & 0 & \sqrt[3]{\frac{1}{\gamma_1\gamma_2}} \end{bmatrix}.$$

The angles α_1 and α_2 are considered in the interval $[0, 2\pi]$ since, in the considered parametrization, K is 2π-periodic with respect to these angles. As observed in the 2D setting, $R^{-1} = R^\top$ since R is a rotation matrix; moreover, the multiplicative coefficient η can be added to balance the magnitude of the diffusion with respect to the other effects, when the transport or the reaction terms are present.

To parametrize the transport $\mathbf{b}$ in 3D domains, we use spherical coordinates, i.e.,

$$\mathbf{b}(\varphi_1, \varphi_2, r) = (r\cos(\varphi_1)\sin(\varphi_2), r\sin(\varphi_1)\sin(\varphi_2), r\cos(\varphi_2))^\top$$

where $\varphi_1 \in [0, 2\pi]$ is the angle between $\mathbf{b}$ and the p_1-axis, $\varphi_2 \in [0, \pi]$ is the angle between $\mathbf{b}$ and the p_3-axis, and $r \in [0, +\infty)$ represents the module of $\mathbf{b}$.

4 | SIMULATION STUDIES

This section is dedicated to simulations, carried out considering simple configurations, that are helpful to understand the performance of the proposed approach.

4.1 | Simulation 1: diffusion estimation

In this first test case, we generate 30 two-dimensional Gaussian random fields with Matérn covariance characterized by different anisotropies, on a square domain with side length equal to 1. The Gaussian random fields are generated through the utility `RFsimulate` available from the R package `RandomFields` (Schlather, Malinowski, Menck, Oesting, & Strokorb, 2015; Schlather et al., 2017), considering angles and eigenvalues ratios randomly sampled from the intervals $[0, \pi]$ and $[2, 5]$. The smoothness parameter ν of the Matérn covariance is set equal to 2. A similar simulation study was considered by Bernardi et al. (2018). We here consider this simple generating scheme as we would like to test the ability of the proposed method to correctly estimate the anisotropy in data, in a context where the data show a clear and known anisotropic pattern. Moreover we can here compare the estimates obtained by the proposed approach, with those provided by anisotropic kriging with a Matérn variogram. The latter method constitutes the golden standard in this setting, since it employs the very same covariance structure that was used to generate the data. Notice that, to assess the goodness of the proposed approach in capturing the correct anisotropy, one has to compare K with $A^\top A$, where A is the Matérn anisotropy matrix. For anisotropic kriging, in order to avoid convergence issues, we consider a diffusion parameter initialization within the ranges exploited for the data generation.
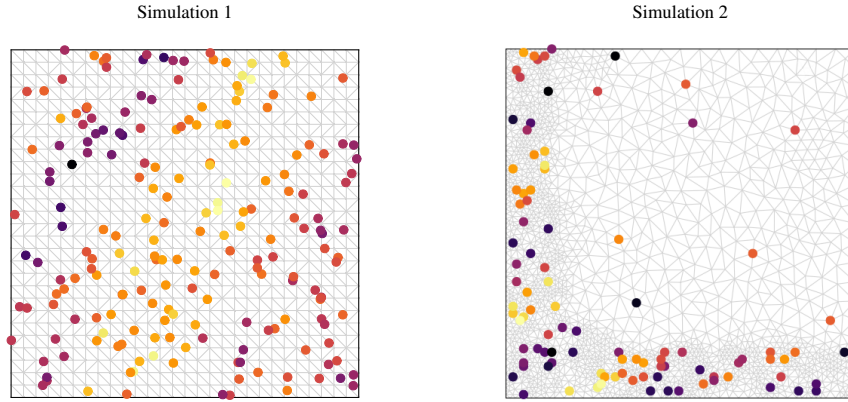
FIGURE 4 Left: Simulation 1. Training data sampled from a Gaussian random field with Matérn covariance (first simulation replicate), and regular mesh used in SR-PDE. Right: Simulation 2. Training data sampled from the solution of a PDE (first simulation replicate), and data-adaptive mesh used in SR-PDE. The color of the markers are related to sampled values.

From each generated field, we create a training and a test dataset. The training dataset is composed of 200 values, observed at 200 locations uniformly sampled within the domain, as displayed in Figure 4, left panel; Gaussian noise, with zero mean and standard deviation equal to 0.1 (which corresponds approximately to 5% of the data range), is added to the true field values. The testing dataset consists of the true field values, on a fine grid of 100×100 locations, on a regular lattice.

We consider the proposed SR-PDE model with unknown diffusion K, while we set **b** and c to zero, in order to focus on diffusion estimation only. The squared domain is discretized through a regular mesh with 346 nodes, displayed in the left panel of Figure 4. This mesh is obtained by the mesh generation and mesh refinement utilities in the `fdaPDE` package (Arnone et al., 2024). We then estimate the diffusion tensors K via the parameter cascading approach described in Section 3, using the same package.

We compare the proposed SR-PDE($\hat{K}, \mathbf{0}, 0$) model to the isotropic SR-PDE($I, \mathbf{0}, 0$) model, to isotropic and anisotropic kriging with Matérn variograms, and to isotropic sPDE approach based on INLA. The isotropic kriging results are computed with the R package `gstat` (Pebesma, 2004). Anisotropic kriging is performed using the R package `geoR` (Diggle & Ribeiro, 2007; Jr & Diggle, 2001). The sPDE approach is implemented using the package R-INLA (www.r-inla.org; Lindgren et al., 2011; Martins, Simpson, Lindgren, & Rue, 2013; Rue et al., 2009) using the built-in utilities to construct a mesh with 415 nodes and considering the default smoothness value $\nu = 1$.

Figure 5 shows the Root Mean Squared Error (RMSE) committed on test data by the different methods, across the 30 simulation replicates. Thanks to the correct diffusion estimates provided by parameter cascading, SR-PDE($\hat{K}, \mathbf{0}, 0$) provides lower RMSE with respect to SR-PDE($I, \mathbf{0}, 0$), isotropic kriging and sPDE approach. Moreover, the RMSE committed by SR-PDE($\hat{K}, \mathbf{0}, 0$) is comparable with that of anisotropic kriging, which is the golden standard in this simulation setting, since it exploits the same covariance structure used to generate the data. Figure 5 also compares the anisotropic diffusion estimates, provided by the proposed approach, and anisotropic kriging: the diffusion angles are sharply captured by SR-PDE($\hat{K}, \mathbf{0}, 0$), with errors comparable to those of anisotropic kriging. Considering the diffusion shape parameters, the results obtained by the proposed approach are less accurate than those of the golden standard. However, this lack of precision in the estimation of γ does not affect the final goodness of fit, since the RMSE obtained by SR-PDE($\hat{K}, \mathbf{0}, 0$) is not significantly different from that of anisotropic kriging, and is lower than that of other competing models. This corroborate the findings in Bernardi et al. (2018), which show that, whenever the optimal angle α is fixed, the SSE does not present a sharp minimum with respect to γ.

Figure 6 offers a visualization of the obtained results, relative to the first sampled random field of this simulation study. The top-left panel shows the test data and the underlying ground truth anisotropy ellipse; the other panels display the predictions and the diffusion estimates provided by different models. In particular, the top-right panel of the figure shows that the proposed parameter cascading procedure returns an accurate estimation of the anisotropy, resulting in precise predictions for SR-PDE($\hat{K}, \mathbf{0}, 0$). Figure 7 compares, instead, the coverage and the amplitude of 95% prediction intervals, on a 100×100 lattice
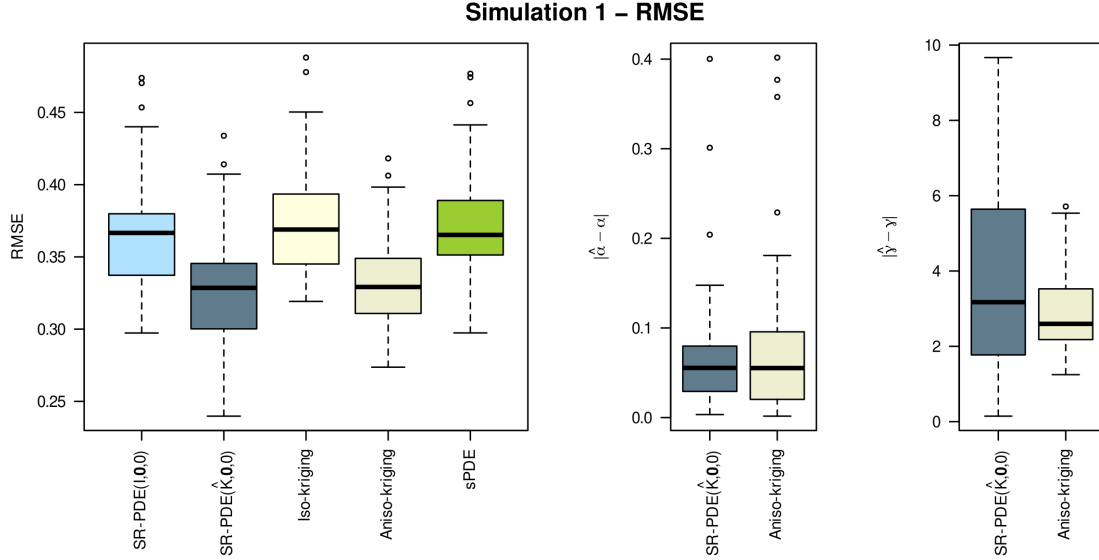
FIGURE 5 Simulation 1. Left: RMSE committed on test data by isotropic and anisotropic SR-PDE, indicated respectively by SR-PDE$(I, \mathbf{0}, 0)$ and SR-PDE$(\hat{K}, \mathbf{0}, 0)$, isotropic and anisotropic kriging, and isotropic sPDE approach based on INLA. Center and right: errors committed by anisotropic SR-PDE and anisotropic kriging, in the estimation of the anisotropy angle α and of the intensity γ. The errors are computed as $|\hat{\alpha} - \alpha|$ and $|\hat{\gamma} - \gamma|$, where $\hat{\alpha}$ and $\hat{\gamma}$ are the estimated parameters, while α and γ are the ground truth values used in the data generation process.

of test locations, across the 30 simulation replicates. These boxplots highlight that the anisotropic SR-PDE$(\hat{K}, \mathbf{0}, 0)$ has similar prediction performances to the golden standard anisotropic kriging, with higher coverage and narrower prediction intervals than isotropic methods.

4.2 | Simulation 2: transport estimation

The second simulation study concerns a setting where there is a strong transport effect. The spatial fields are here generated solving diffusion-transport-reaction PDEs, using the software FEniCS (Alnaes et al., 2015), on a square domain with side length equal to 1. To explore different scenarios, we compute 30 different PDE solutions, considering random transport vectors, with angles and magnitude uniformly sampled in $[0, 2\pi]$ and $[500, 1000]$, respectively; moreover, we set $K = I$ and $c = 0$. The transport intensities are larger than the diffusion intensity, in order to emphasize the transport effect over the diffusion one. To avoid trivial solutions, the source term is set equal to $u = 500 \cos(20y^2) + 500 \cos(20x^2)$, while Dirichlet boundary conditions are exploited to set the value of f equal to $\cos(5\pi x)$ and $\cos(5\pi y)$, respectively, on the horizontal and on the vertical side of the inflow boundary.

For each PDE solution, we create a training and a test dataset. The training dataset is composed of 90 observations, measured at random locations, near the left and the bottom side of the domain, with only 10 additional values observed in the remaining portion of the domain, as visible in the right panel of Figure 4. This inhomogeneous pattern of measurements can be observed in several environmental problems, such as for instance in applications to buoy data, since buoys are moored in shallow waters, close to the coastlines that constitute the boundaries of the domain of interest. A Gaussian noise with zero mean and standard deviation equal to 0.1, which corresponds approximately to 5% of the data range, is added to the training data. The test data is composed of measures of the PDE solution at a fine grid of 100×100 points over the square domain.

We here illustrate the ability of the proposed model to leverage on partial information about the phenomenon under study. Specifically, we assume that the phenomenon is characterized by a transport effect, though we do not impose neither the direction nor the intensity of this transport term. We thus consider a SR-PDE$(I, \hat{\mathbf{b}}, 0)$ model, where the unknown transport term is
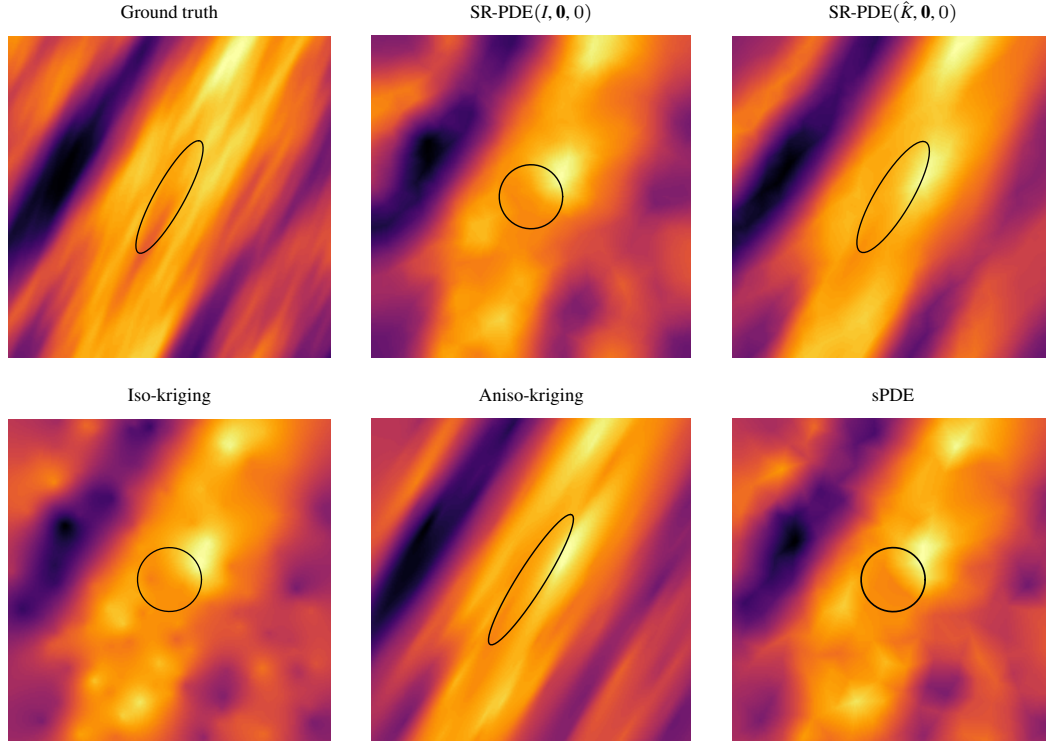
FIGURE 6 Simulation 1. Top left: first test field; the ellipse visualizes the true anisotropy of the field. Other panels: field estimates provided by the competing methods, with the corresponding anisotropy ellipses. The competing models are isotropic and anisotropic SR-PDE, indicated respectively by SR-PDE($I, \mathbf{0}, 0$) and SR-PDE($\hat{K}, \mathbf{0}, 0$), isotropic and anisotropic kriging, and isotropic sPDE approach based on INLA.

FIGURE 7 Simulation 1. Coverage (left) and amplitude (right) of 95% prediction intervals, on a 100×100 lattice of test locations, across the 30 simulation replicates. The competing models are isotropic and anisotropic SR-PDE, indicated respectively by SR-PDE($I, \mathbf{0}, 0$) and SR-PDE($\hat{K}, \mathbf{0}, 0$), isotropic and anisotropic kriging, and isotropic sPDE approach based on INLA.
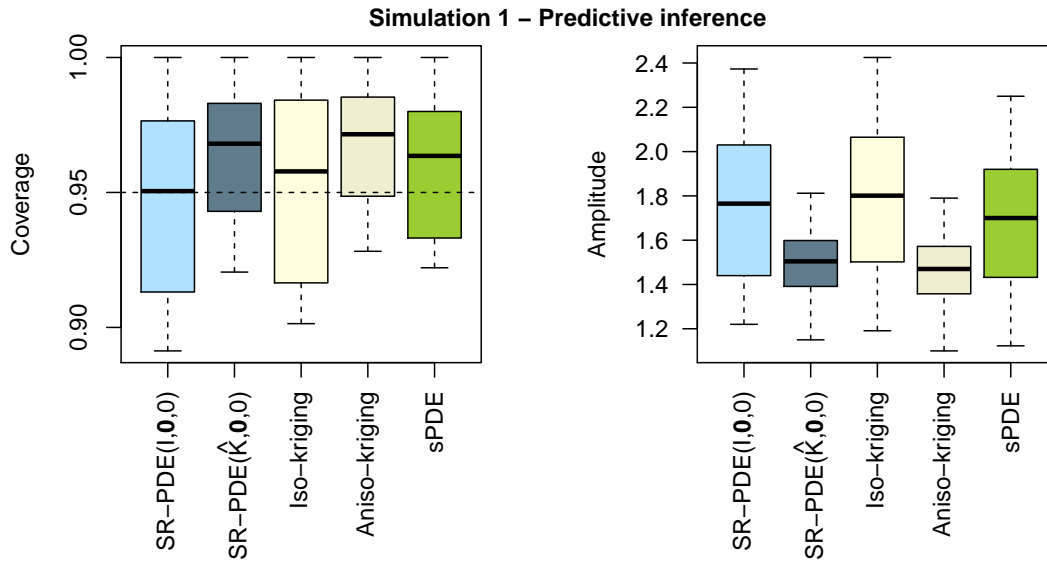
estimated via the parameter cascading approach described in Section 3. As done for Simulation 1 and for the applications presented in Section 5 and 6, we consider null forcing term and homogeneous Neumann conditions; we thus use a different forcing term and different boundary conditions with respect to those that were used to generate the data. Since the training data locations are strongly inhomogeneous in space, we apply a mesh adaptivity procedure, as suggested by Ferraccioli, Arnone, Finos, Ramsay, and Sangalli (2021), to enable more flexibility in the estimation where we have more data, while saving computational cost. In particular, we consider a Voronoi tessellation of the training data locations: this is a partition of the spatial domain where the i-th subdomain is the set of points that are closer to the i-th training data location than to any other data location in the training set. Starting from the Voronoi vertices, we then create the mesh using the mesh generation and mesh refinement utilities of the `fdaPDE` package. This results in meshes that are finer where more training data are observed, as displayed in the right panel of Figure 4 concerning the first simulation replicate, and with an average of 1643 nodes.

We also compute the estimates given by isotropic SR-PDE, SR-PDE($\hat{K}, \mathbf{0}, 0$), isotropic and anisotropic kriging with Matérn variograms, and isotropic sPDE approach based on INLA with a mesh having 1595 nodes. These methods are implemented using the same packages indicated in Section 4.1.

Figure 8 shows the boxplots of the RMSE committed on test data by the different methods, across the 30 simulation replicates. The proposed SR-PDE($I, \hat{\mathbf{b}}, 0$) returns by far the smallest RMSE. Even though the training data are concentrated in a small region of the domain, the transport angles are estimated with a good accuracy, with a median error of about 0.067 radians and a maximum error of about 0.137 radians. The results on the magnitude of the transport are less sharp, but this does not influences the overall quality of the estimation, as already highlighted in Section 4.1. Figure 9 illustrates the predictions provided by the considered models in the first simulation replicate. In particular, the top right panels depict the differences between the effect of an anisotropic diffusion term and of a transport term. The transport estimated by the proposed SR-PDE($I, \hat{\mathbf{b}}, 0$) model provides a very good estimate of the true transport vector. As a result, despite of the small sample size and the strongly inhomogeneous pattern of the data locations, the spatial field estimated by SR-PDE($I, \hat{\mathbf{b}}, 0$) follows faithfully the ground truth patter. Notice that this model employs wrong forcing term and wrong boundary conditions. Nevertheless, the ability of the proposed method to accurately retrieve the underlying physics leads to remarkably good predictions, even in regions of the domain with few training data. Instead, the estimates provided by the competing methods are unable to capture the overall spatial pattern, as also confirmed by the markedly higher RMSE shown in the left panel of Figure 5. Figure 10 compares the coverage and the amplitude of 95% prediction intervals, on a 100×100 lattice of test locations, across the 30 simulation replicates. Thanks to the reliable estimate of the PDE obtained through parameter cascading, the proposed SR-PDE($I, \hat{\mathbf{b}}, 0$) is able to return very accurate predictions, with narrow intervals, even in this setting characterized by few data. These results emphasize the importance of properly using the available physical knowledge in order to face challenging data analysis with complex spatial patterns. Moreover, when the data locations are strongly inhomogeneous over the spatial domain, the use and accurate estimation of a suitable problem-specific description can be very helpful in order to extrapolate good predictions over the whole domain. This aspect will be further illustrated by the application to buoy data in Section 6.

5 | SWITZERLAND RAINFALL

This section is dedicated to the application to rainfall data in Figure 1. The dataset comprises 467 daily rainfall measurements, recorded in Switzerland on May 8, 1986. This dataset was used for the Spatial Interpolation Comparison 97 (`ftp://ftp.geog.uwo.ca/SIC97/intro/alldata.dat;` Dubois et al., 2003). Heavy and prolonged precipitations are the main driver of flooding in Switzerland. By understanding rainfall patterns, and where the heaviest rainfall is likely to occur, it is possible to develop better flood forecasting systems, and design more effective flood prevention measures. Moreover, rainfall monitoring is helpful to manage water resources.

As visible from Figure 1, the spatial distribution of collected rainfall data is strongly anisotropic, possibly due to the complex interaction between geomorphology and atmospheric circulation. This anisotropic pattern cannot be explained by covariates, such as elevation, which turn out to be not significant in a regression setting, as demonstrated by Bernardi et al. (2018) and Ferraccioli et al. (2022). Unfortunately, we lack here a detailed PDE description of this physics, that could be used to inform the estimator. Nevertheless, in SR-PDE modeling, we can use a stationary anisotropic diffusion term, with unknown direction and intensity, to model the apparent anisotropy in the data. Moreover, we might expect that the rainfall was accompanied by wind. If we had some information on the wind in Switzerland on May 8, 1986, we could have encoded such knowledge in an appropriate transport term $\mathbf{b}$. Since we could not find any record on the wind on that day, we include in the SR-PDE model a stationary
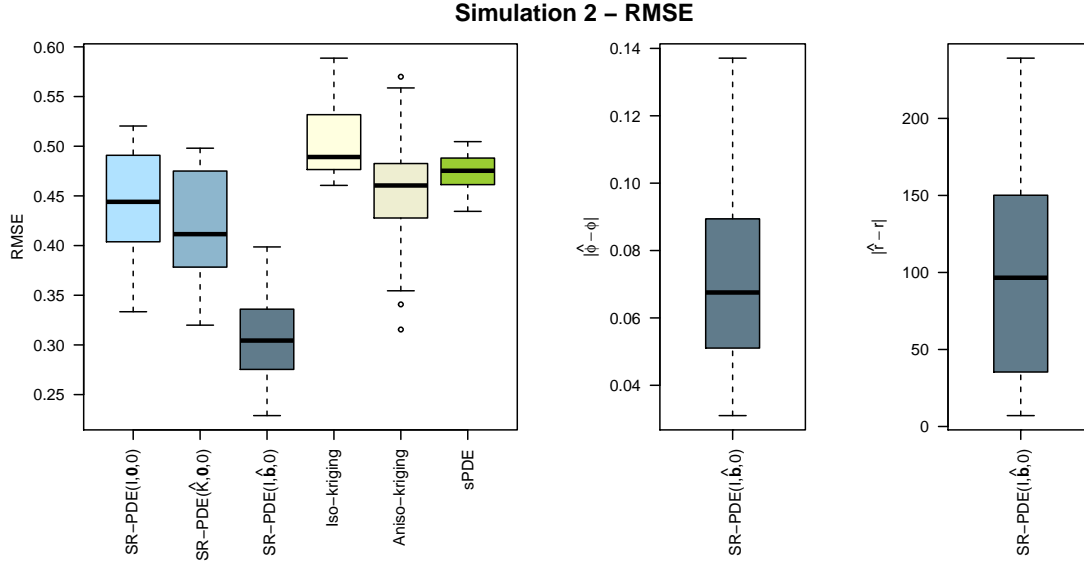
FIGURE 8 Simulation 2. Left: RMSE committed on test data by isotropic and anisotropic SR-PDE, indicated respectively by SR-PDE($I, \mathbf{0}, 0$) and SR-PDE($\hat{K}, \mathbf{0}, 0$), SR-PDE with unknown transport, indicated by SR-PDE($I, \hat{\boldsymbol{b}}, 0$), isotropic and anisotropic kriging, and isotropic sPDE approach based on INLA. Center and right: estimation errors committed by anisotropic SR-PDE when estimating the transport angle φ and the intensity r, with respect to the ground truth values. The errors are computed as $|\hat{\varphi} - \varphi|$ and $|\hat{r} - r|$, where $\hat{\varphi}$ and $\hat{r}$ are the estimated parameters, while φ and r are the ground truth values used in the data generation process.

transport term with unknown direction and intensity. Finally, we set a null reaction term, since no meaningful shrinkage effect can be envisioned in this applied problem.

We use the regular triangulation of the Swiss territory, having 1127 nodes, shown in the right panel of Figure 1. The optimal diffusion parameters found via iterative parameter cascading are $\hat{\alpha} = 2.454$ radians and $\hat{\gamma} = 6.001$, while the transport ones are $\hat{\varphi} = 0.917$ radians and $\hat{r} = 6.9378$. The top-right panel of Figure 11 shows the estimated optimal diffusion ellipse $\hat{K}$ and transport vector $\hat{\mathbf{b}}$: they follow faithfully the spatial pattern of the rainfall data. Remarkably, the optimal transport estimated is also perfectly aligned with respect to the mean wind speed rose observed in Switzerland over a 10 years period (2008-2017), provided by Davis et al. (2019).

Figure 11 displays the estimate of the rainfall in Switzerland provided by the considered SR-PDE($\hat{K}, \hat{\mathbf{b}}, 0$), compared to the estimates provided by the following competing methods: isotropic SR-PDE; anisotropic SR-PDE($\hat{K}, \mathbf{0}, 0$), which does not include information on the prevailing wind; isotropic and anisotropic kriging with Matérn variograms; sPDE approach based on INLA with a mesh having 1265 nodes. The various methods are implemented through the same utilities introduced in Section 4.1. The bottom-right panel of Figure 11 shows leave-one-out Cross-Validation (CV) errors of the different spatial models. SR-PDE($\hat{K}, \hat{\mathbf{b}}, 0$) has significant lower CV errors than all the other methods. In particular, if the transport vector is estimated, along with the diffusion matrix, the results improve not only with respect to SR-PDE($I, \mathbf{0}, 0$), i.e., with respect to the isotropic SR-PDE model, but also with respect to the SR-PDE($\hat{K}, \mathbf{0}, 0$) model proposed by Bernardi et al. (2018), that enabled only the estimation of the diffusion term.

6 | BUOY DATA AROUND FLORIDA PENINSULA

This section focuses on the analysis of the oceanographic data illustrated in the top panels of Figure 2. In particular, we consider sea surface temperatures and dissolved oxygen, measured at moored buoys in the Gulf of Mexico, around the coastlines of the Florida peninsula on April 1, 2020. Temperature and oxygen data are made freely available by the National Oceanic and Atmospheric Administration (NOAA), respectively at `https://www.ndbc.noaa.gov` (National Data Buoy Center, 2023) and
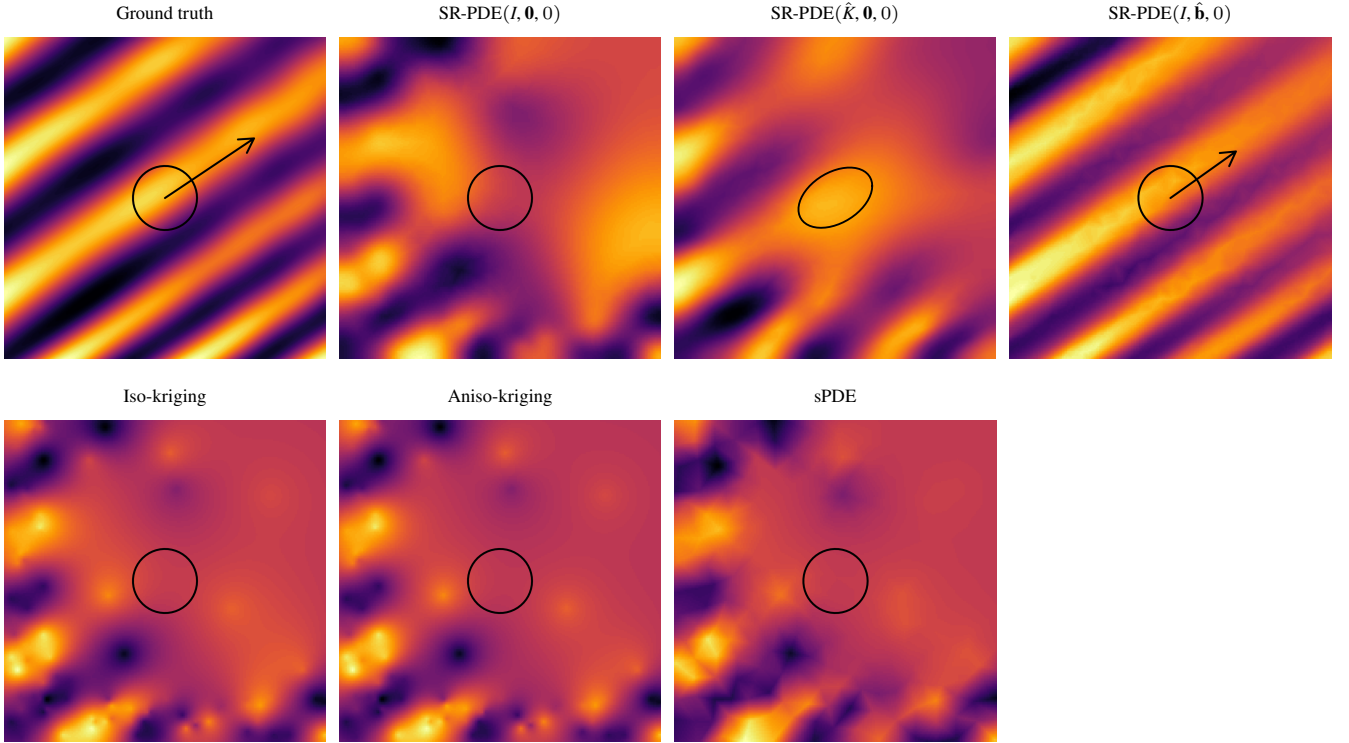
FIGURE 9 Simulation 2. Top left: heatmap of the first test field; the vector visualizes the true transport of the field. Other panels: heatmaps of the predicted spatial fields, with the corresponding anisotropy ellipses. The competing models are isotropic and anisotropic SR-PDE, indicated respectively by SR-PDE$(I, \mathbf{0}, 0)$ and SR-PDE$(\hat{K}, \mathbf{0}, 0)$, SR-PDE with unknown transport, indicated by SR-PDE$(I, \hat{\boldsymbol{b}}, 0)$, isotropic and anisotropic kriging, and isotropic sPDE approach based on INLA. For SR-PDE$(I, \hat{\boldsymbol{b}}, 0)$, displayed in the top-right panel, also the estimated transport term is displayed.
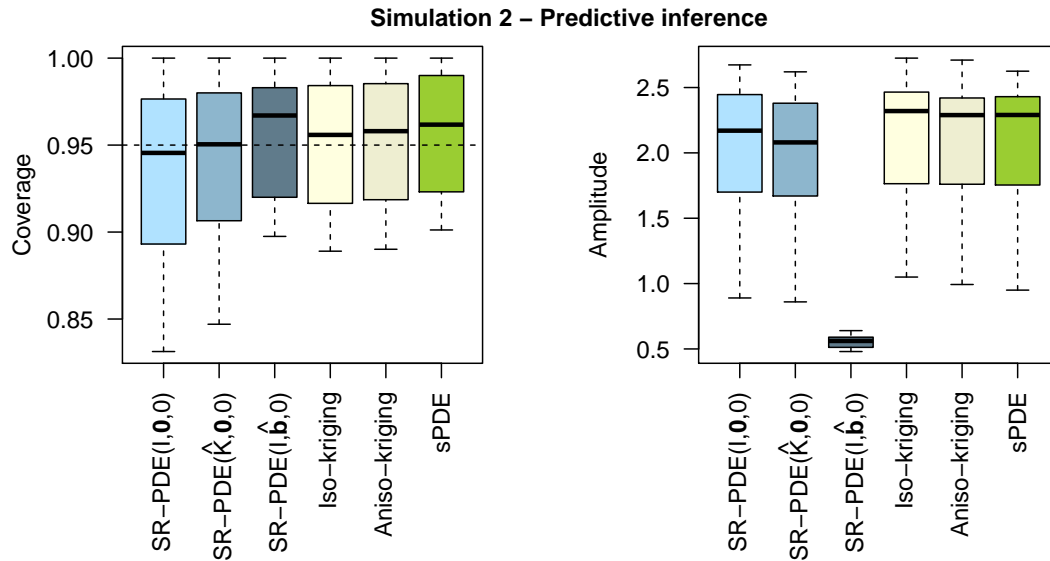

FIGURE 10 Simulation 2. Coverage (left) and amplitude (right) of 95% prediction intervals, on a 100×100 lattice of test locations, across the 30 simulation replicates. The competing models are isotropic and anisotropic SR-PDE, indicated respectively by SR-PDE$(I, \mathbf{0}, 0)$ and SR-PDE$(\hat{K}, \mathbf{0}, 0)$, SR-PDE with unknown transport, indicated by SR-PDE$(I, \hat{\boldsymbol{b}}, 0)$, isotropic and anisotropic kriging, and isotropic sPDE approach based on INLA.
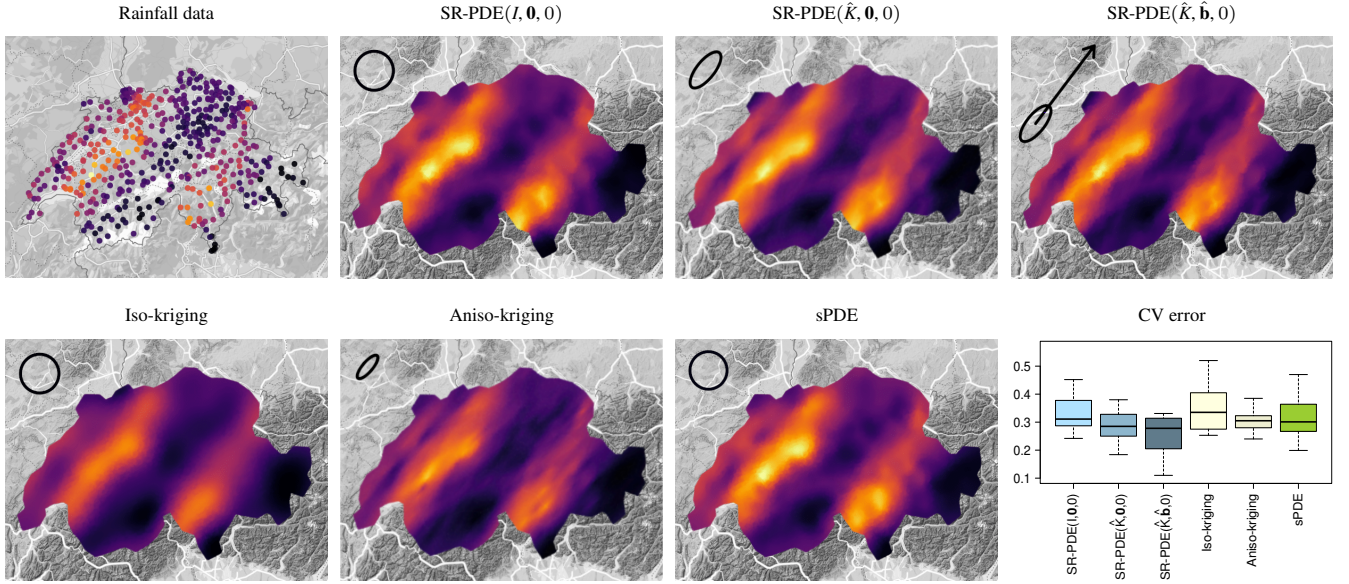
FIGURE 11 Switzerland rainfall data. Top left: rainfall data measured at different locations of the Swiss territory. Bottom right: leave-one-out cross-validation errors committed by different methods. Other panels: spatial field estimates of rainfall in Switzerland provided by different competing methods, with the corresponding anisotropy ellipse. The competing models are: isotropic SR-PDE, anisotropic SR-PDE and anisotropic SR-PDE with unknown transport, indicated respectively by SR-PDE$(I, \mathbf{0}, 0)$, SR-PDE$(\hat{K}, \mathbf{0}, 0)$ and SR-PDE$(\hat{K}, \hat{\mathbf{b}}, 0)$; isotropic and anisotropic kriging; isotropic sPDE approach based on INLA. For SR-PDE$(\hat{K}, \hat{\mathbf{b}}, 0)$, displayed in the top-right panel, also the estimated transport term, which captures the prevailing wind on the day of the records, is displayed.

`www.ncei.noaa.gov/archive/accession/NCEI-WOA18` (Boyer et al., 2018). The non-trivial form of the spatial domain, characterized by the presence of the Florida peninsula, highly influences the oceanographic quantities under study. Indeed, for example, the temperatures observed at two buoys on opposite sides of the Florida peninsula, are naturally less associated than the temperatures observed at two buoys, at equal distance, but located on the same side of the peninsula. Moreover, the phenomenon under study is strongly characterized by the Gulf Stream, that is a warm, swift and non-stationary Atlantic Ocean current, shown in the bottom-right panel of Figure 2. It is thus particularly desirable to analyse these data using a method capable to take into account this physical knowledge. The SR-PDE modeling framework is well suited to model these data. Indeed, on the one hand, it naturally accounts for the non-trivial shape of the domain. On the other hand, the influence of the Gulf Stream on the spatial distribution of the considered oceanographic quantities can be properly captured by a diffusion-transport PDE, with a stationary isotropic diffusion, combined with a space-varying transport function $\mathbf{b}(\mathbf{p})$, that represents the Gulf Stream velocity in each location of the domain. In particular, the direction and intensity of the Gulf Stream around Florida are provided by the Ocean Surface Current Analysis Real-time (OSCAR) dataset, with a 5-day resolution (Earth Space Research, 2009). OSCAR provides near-surface ocean current estimates derived using quasi-linear and steady flow momentum equations, applied to satellite-sensed data concerning ocean wind, sea surface temperature and height gradients. Since we do not know a priori the relative intensities of the diffusion and transport terms, we let the intensity parameter η of the diffusion term be unspecified, and we estimate it using the parameter cascading approach detailed in Section 3. The reaction coefficient can instead be set to zero, since the shrinkage effect is not meaningful for the phenomenon under study.

For the implementation of SR-PDE, we use the data-adaptive mesh, with 1635 nodes, shown in the bottom-right panel of Figure 2. In transport-dominated settings, such as the one here considered, data-driven meshes, besides saving computational cost, may also prevent possible numerical instabilities, that may result from the strong transport. Specifically, the data-driven mesh has been obtained starting from a fine mesh, and then applying a rejection sampling procedure to get a coarser triangulation where the magnitude of the velocity $\mathbf{b}$ is low: the smaller the Gulf Stream intensity at a mesh node, the higher the probability of deleting that node from the triangulation.

Mean (st. dev.) of CV errors	01/04/2020	01/10/2020	01/04/2021	01/10/2021	01/04/2022	01/10/2022
SR-PDE($I, \mathbf{0}, 0$)	0.789 (0.324)	0.812 (0.346)	0.597 (0.283)	0.884 (0.325)	0.731 (0.284)	0.821 (0.337)
SR-PDE($\hat{K}, \mathbf{b}, 0$)	**0.391 (0.167)**	**0.282 (0.152)**	**0.270 (0.135)**	**0.368 (0.207)**	**0.499 (0.197)**	**0.393 (0.169)**
Iso-kriging	0.991 (0.342)	1.004 (0.484)	0.655 (0.278)	1.203 (0.288)	1.134 (0.314)	0.930 (0.453)
Aniso-kriging	0.700 (0.450)	0.721 (0.356)	0.533 (0.304)	0.821 (0.324)	0.750 (0.400)	0.839 (0.485)
sPDE	0.639 (0.258)	0.603 (0.361)	0.556 (0.213)	0.830 (0.288)	0.744 (0.311)	0.678 (0.296)

T A B L E 1   Sea Surface Temperature (SST) around Florida peninsula. Mean leave-one-out cross-validation errors and corresponding standard deviations committed by different methods on SST data measured at five different days. The competing methods are: the isotropic SR-PDE($I, \mathbf{0}, 0$); the proposed SR-PDE($\hat{K}, \mathbf{b}, 0$), which includes information of the Gulf Stream in the transport $\mathbf{b}$ and uses the parameter cascading approach in Section 3; isotropic and anisotropic kriging; sPDE approach based on INLA, using the barrier model.

6.1 | Target: sea surface temperature

The modeling and monitoring of Sea Surface Temperatures (SST) is essential for marine ecosystems and weather forecasting. For instance, SST affects the distribution of life underwater, since warm seawater supports the presence of plankton, plants and fish. SST also influences the formation of clouds and precipitation, because the heat exchange, between the ocean and the atmosphere, drives atmospheric circulation. Moreover, SST is a key metric for monitoring climate change, as the ocean absorbs over 90% of the surplus heat caused by human-induced climate change.

We model SST by a SR-PDE model with the regularizing PDE described above. The parameter cascading approach in Section 3 returns the estimate $\hat{\eta} = 0.0218$ for the diffusion intensity. This small optimal value for the diffusion intensity η suggests that the transport has a very significant impact on the phenomenon under study, and it dominates over the diffusion effect.

Figure 12 displays the estimate of SST provided by the considered SR-PDE($\hat{K}, \mathbf{b}, 0$), compared to the estimates provided by the following competing methods: isotropic SR-PDE, which does not include information on the Gulf Stream; isotropic and anisotropic kriging with Matérn variograms; sPDE approach considering the barrier model presented in Bakka et al. (2019) with a mesh having 1800 nodes. The bottom-right panel of the same figure displays the boxplots of leave-one-out cross-validation errors for the various methods: SR-PDE($\hat{K}, \mathbf{b}, 0$) attains significant lower errors than all other methods.

The top-right panel of Figure 12 also displays the SST field provided by NASA satellite images (JPL MUR MEaSUREs Project, 2015). It is important to notice that these data are not used in the estimation. They are here displayed only to enable comparison with respect to the SST estimates provided by the competing methods, on the basis of the buoy data. Such visual comparison highlight that none of the competing methods, apart from the proposed SR-PDE($\hat{K}, \mathbf{b}, 0$), can capture the strongly anisotropic and non-stationary pattern of SST. The proposed method, leveraging on the available problem-specific information concerning the presence of the Gulf Stream, is capable instead to very well estimate the spatial pattern of the quantity under study, to a highly remarkable level of detail, using solely the measurements at the buoys. Indeed, thanks to the inclusion of a suitable space-varying transport term, and to the optimal estimation of η given by the proposed parameter cascading, SR-PDE($\hat{K}, \mathbf{b}, 0$) can capture the strongly anisotropic and non-stationary features that are apparent from the satellite images.

To further assess the performance of the proposed approach, and to provide a wider comparison with respect to the competing methods, we consider additional SST buoy data, measured at dates in spring and autumn, every 6 months from the date considered in Figure 12. Table 1 shows the resulting means and standard deviations of leave-one-out CV errors for the competing models, confirming the superiority of the proposed technique.

These results highlight that a suitable physical description of the problem under study is crucial in the estimation, especially when dealing with complex problems strongly characterized by a physical phenomenon such as the Gulf Stream.

6.2 | Target: dissolved oxygen

We now consider another fundamental oceanographic quantity, Dissolved Oxygen (DO), that is one of the main indicators of aquatic ecosystems health. DO is essential for the survival of fish, invertebrates and bacteria, since a depletion of DO results in the suffocation of aquatic organisms. In addition, the presence of DO plays a key role in enhancing the water quality: indeed, bacteria take advantage of DO to decompose organic matter, such as sewage and algae blooms; therefore, when DO levels are
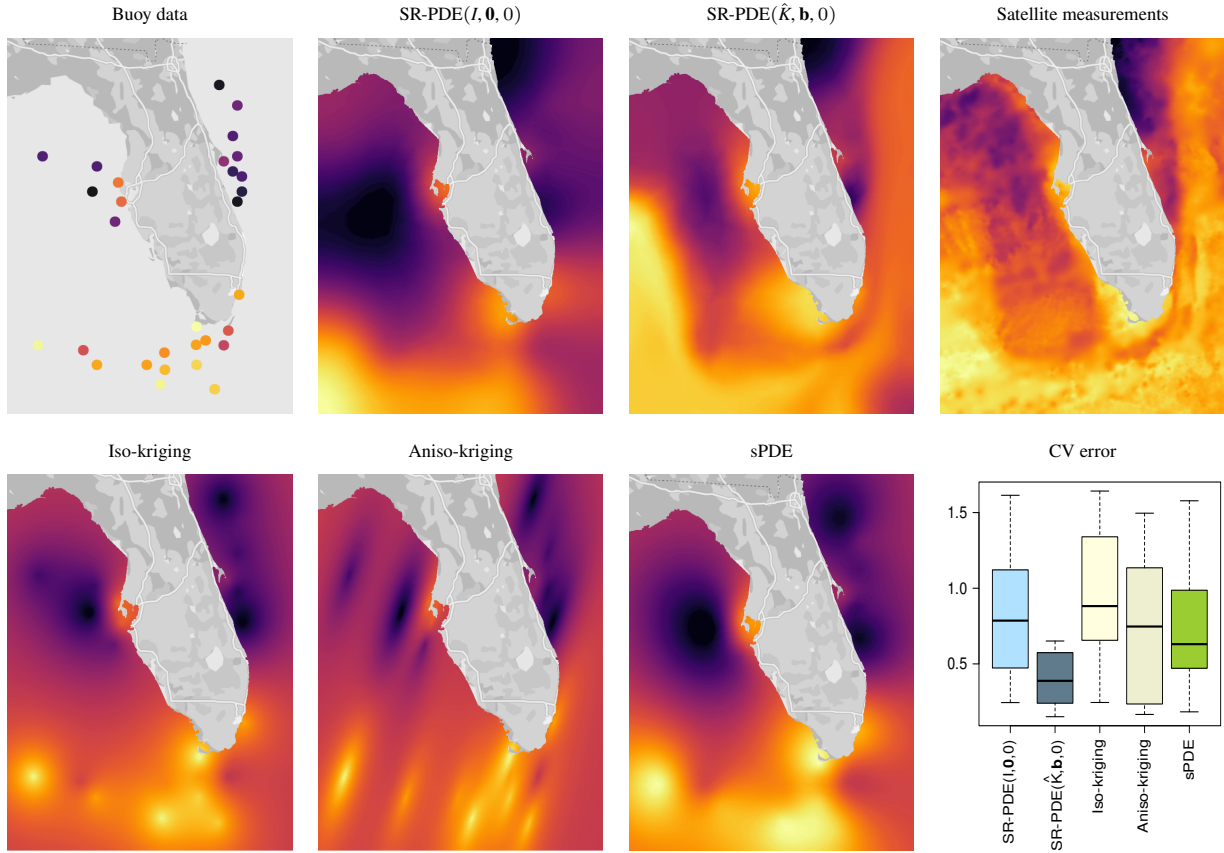
FIGURE 12 Sea Surface Temperature (SST) around Florida peninsula. Top left: SST measured at moored buoys, located around the Florida coastlines. Top right: SST provided by NASA satellite images; these data are not used to compute the estimates, and are here displayed only to enable comparison with the estimates provided by the considered competing methods. Bottom right: leave-one-out cross-validation errors, committed by different methods. Other panels: SST estimates provided by the considered competing methods. The competing methods are: the isotropic SR-PDE$(I, \mathbf{0}, 0)$; the anisotropic SR-PDE$(\hat{K}, \mathbf{b}, 0)$, which includes information of the Gulf Stream in the transport $\mathbf{b}$ and uses the parameter cascading approach in Section 3; isotropic and anisotropic kriging; sPDE approach based on INLA, using the barrier model.

insufficient, organic matter can accumulate and lead to water pollution. For these reasons, modeling and monitoring the spatial behaviour of the DO concentration in seawater is crucial to identify and address environmental problems early on.

We model DO, using SST as a covariate. DO is in fact highly negatively correlated with SST, with a Pearson correlation index equal to –0.713. This is due to the fact that warm water provokes a leakage of oxygen, due to the faster movements of the molecules. Specifically, we consider a SR-PDE$(\hat{K}, \mathbf{b}, 0)$ model, with the same PDE described above (with unknown intensity of the diffusion term), and used to model SST in Section 6.1. Such PDE provides a valid model for most oceanographic quantities measured at buoys. We use the same data-driven mesh shown in the bottom-right panel of Figure 2. Applying the parameter cascading algorithm in Section 3, we obtain $\hat{\eta} = 0.07$; this value is of the same order of magnitude than that estimated in Section 6.1, leading to the same balance between diffusion and transport. Indeed, if we had used the same PDE parameter estimated in Section 6.1, we would have obtained estimates having totally comparable leave-one-out cross-validation errors, as tested by Wilcoxon test. This confirms that the PDE provides an overall very accurate description for the spatial variation of the oceanographic quantities under study. The fitted SR-PDE$(\hat{K}, \mathbf{b}, 0)$ model returns a $\hat{\beta}$ coefficient equal to –0.756, with an approximate 95% Wald confidence interval for β given by $(-0.882, -0.629)$, coherently with the negative correlation between DO and SST mentioned above.
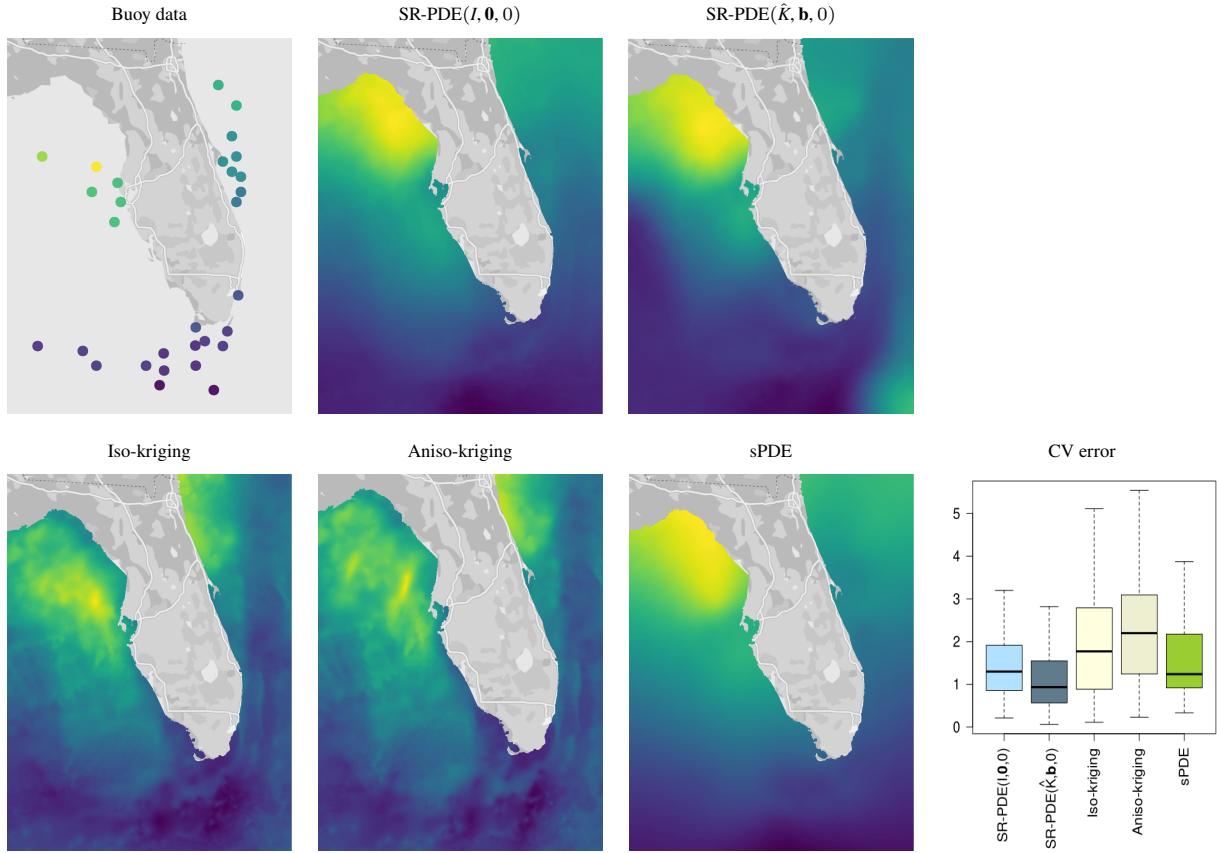
FIGURE 13 Dissolved Oxygen (DO) around Florida peninsula. Top left: DO concentration measured at moored buoys, located around the Florida coastlines. Bottom right: leave-one-out cross-validation errors committed by different competing methods. Other panels: DO concentration estimates provided by different competing methods. The competing methods are: the isotropic SR-PDE($I, \mathbf{0}, 0$); the proposed SR-PDE($\hat{K}, \mathbf{b}, 0$), which includes information of the Gulf Stream in the transport $\mathbf{b}$ and uses the parameter cascading approach in Section 3; isotropic and anisotropic kriging; sPDE approach based on INLA, using the barrier model.

Figure 13 shows the estimates of DO fields predicted by different competing models, all including SST as covariate. The competing methods are the same considered in Section 6.1. The same figure also displays, in the bottom-right panel, the leave-one-out cross-validation errors for the competing methods. Also in this application, the proposed SR-PDE($\hat{K}, \mathbf{b}, 0$) attains the lower cross-validation errors values. In particular, the mean leave-one-out cross-validation error provided by SR-PDE($\hat{K}, \mathbf{b}, 0$) is about 4% of the range of the observed DO values, whilst those of competing models range between 6% and 10%. The proposed method thus confirms its very good performances.

7 | CONCLUSIONS

SR-PDE provides a powerful physics-informed spatial regression framework, that permits to take into account a suitable PDE description of the phenomenon under study. Doing so, both fidelity to the data and fidelity to the physical model contribute to find accurate and robust estimates, that are coherent, not only with the observed data, but also with the available problem-specific information. This is crucial, for instance, when facing environmental problems characterized by data scarcity or inhomogeneity, by complex spatial domains, or strongly non-stationary spatial patterns, such as in the application to buoy data, detailed in Section 6. Indeed, the addition of a physical description of some important aspect of the phenomena under study, such as the presence of the Gulf Stream in the application to buoy measurements, is essential to provide an accurate modeling of the data at hand, and thus a better understanding of the underlying process.

Furthermore, thanks to the parameter cascading approach here described, it is now possible to retrieve appropriate values for the PDE parameters, whenever these cannot be specified on the basis of problem-specific information. This estimation approach permits to fully deploy the power of SR-PDE, even in settings where we lack problem-specific information, or the available information is incomplete. The application to rainfall measurements over Switzerland, in Section 5, offers an illustrative example in this sense: indeed, it shows that we can accurately estimate the unknown anisotropy in the data, as well as retrieve the unknown prevailing wind, leading to estimates superior to those offered by state-of-the art competitors.

There are of course a number of possible extensions of the proposed approach. A very interesting direction of future research concerns generalizations of the parameter cascading procedure in order to retrieve unknown space-varying PDE parameters, in analogy to what described, e.g., by Fuglstad, Lindgren, et al. (2015); Fuglstad, Simpson, et al. (2015), for the sPDE approach. Another interesting further development goes towards space-time data settings, leveraging on the SR-PDE models for space-time data proposed by Arnone et al. (2019) and Arnone, Sangalli, and Vicini (2023). Additional extensions, that would further broaden the applicability of this rich family of physics-informed regression models, concern spatial generalized linear settings, appropriately combining the proposed approach with the functional iterative penalized least square technique described in Wilhelm and Sangalli (2016), as well as the use of fractional differential operators. Finally, a fascinating direction of future research consists in refining the available inference approaches for SR-PDE models with fixed PDE parameters, based on classical Wald inference or on the innovative resampling ideas developed in Ferraccioli et al. (2022, 2023) and Cavazzutti et al. (2024), in order to also account for uncertainty in the PDE parameters.

ACKNOWLEDGMENTS

REFERENCES

Alnaes, M. S., Blechta, J., Hake, J., Johansson, A., Kehlet, B., Logg, A., … Wells, G. N. (2015). The FEniCS Project Version 1.5. *Archive of Numerical Software*, *3*. doi: 10.11588/ans.2015.100.20553

Arnone, E., Azzimonti, L., Nobile, F., & Sangalli, L. M. (2019). Modeling spatially dependent functional data via regression with differential regularization. *Journal of Multivariate Analysis*, *170*, 275–295. Retrieved from `https://www.sciencedirect.com/science/article/pii/S0047259X17307613` Special Issue on Functional Data Analysis and Related Topics. doi: 10.1016/j.jmva.2018.09.006

Arnone, E., Clemente, A., Sangalli, L. M., Lila, E., Ramsay, J., & Formaggia, L. (2024). *fdaPDE: Physics-Informed Spatial and Functional Data Analysis*. `https://CRAN.R-project.org/package=fdaPDE`. R package version 1.1-19.

Arnone, E., Negri, L., Panzica, F., & Sangalli, L. M. (2023). Analyzing data in complicated 3D domains: Smoothing, semiparametric regression, and functional principal component analysis. *Biometrics*. Retrieved from `https://onlinelibrary.wiley.com/doi/abs/10.1111/biom.13845` doi: 10.1111/biom.13845

Arnone, E., Sangalli, L. M., & Vicini, A. (2023). Smoothing spatio-temporal data with complex missing data patterns. *Statistical Modelling*, *23*(4), 327-356. Retrieved from `https://doi.org/10.1177/1471082X211057959` doi: 10.1177/1471082X211057959

Augustin, N. H., Trenkel, V. M., Wood, S. N., & Lorance, P. (2013). Space-time modelling of blue ling for fisheries stock management. *Environmetrics*, *24*(2), 109–119. Retrieved from `https://onlinelibrary.wiley.com/doi/abs/10.1002/env.2196` doi: 10.1002/env.2196

Azzimonti, L., Nobile, F., Sangalli, L. M., & Secchi, P. (2014). Mixed Finite Elements for Spatial Regression with PDE Penalization. *SIAM/ASA Journal on Uncertainty Quantification*, *2*(1), 305–335. Retrieved from `https://doi.org/10.1137/130925426` doi: 10.1137/130925426

Azzimonti, L., Sangalli, L. M., Secchi, P., Domanin, M., & Nobile, F. (2015). Blood Flow Velocity Field Estimation Via Spatial Regression With PDE Penalization. *Journal of the American Statistical Association*, *110*(511), 1057–1071. Retrieved from `https://doi.org/10.1080/01621459.2014.946036` doi: 10.1080/01621459.2014.946036

Bakka, H., Vanhatalo, J., Illian, J. B., Simpson, D., & Rue, H. (2019). Non-stationary Gaussian models with physical barriers. *Spatial Statistics*, *29*, 268–288. Retrieved from `https://www.sciencedirect.com/science/article/pii/S221167531830099X` doi: 10.1016/j.spasta.2019.01.002

Berliner, L. M. (2003). Physical-statistical modeling in geophysics. *Journal of Geophysical Research: Atmospheres*, *108*(D24). Retrieved from `https://agupubs.onlinelibrary.wiley.com/doi/abs/10.1029/2002JD002865` doi: 10.1029/2002JD002865

Bernardi, M. S., Carey, M., Ramsay, J. O., & Sangalli, L. M. (2018). Modeling spatial anisotropy via regression with partial differential regularization. *Journal of Multivariate Analysis*, *167*(C), 15–30. doi: 10.1016/j.jmva.2018.03.01

Bolin, D., & Lindgren, F. (2011). Spatial models generated by nested stochastic partial differential equations, with an application to global ozone mapping. *The Annals of Applied Statistics*, *5*(1), 523–550. Retrieved from `http://www.jstor.org/stable/23024839`

Bonas, M., & Castruccio, S. (2023). Calibration of SpatioTemporal forecasts from citizen science urban air pollution data with sparse recurrent neural networks. *The Annals of Applied Statistics*, *17*(3), 1820–1840. Retrieved from `https://doi.org/10.1214/22-AOAS1683` doi: 10.1214/22-AOAS1683

Bonas, M., Richter, D. H., & Castruccio, S. (2023). *A Physics-Informed, Deep Double Reservoir Network for Forecasting Boundary Layer Velocity.*

Boyer, T. P., García, H. E., Locarnini, R. A., Zweng, M. M., Mishonov, A. V., Reagan, J. R., … Smolyar, I. V. (2018). *World Ocean Atlas 2018. NOAA National Centers for Environmental Information.* `www.ncei.noaa.gov/archive/accession/NCEI-WOA18`. Accessed: 2022-08-29.

Cameletti, M., Lindgren, F., Simpson, D., & Rue, H. (2013). Spatio-temporal modeling of particulate matter concentration through the SPDE approach. *AStA Advances in Statistical Analysis*, *97*(2), 109–131. doi: 10.1007/s10182-012-0196-3

Cavazzutti, M., Arnone, E., Ferraccioli, F., Galimberti, C., Finos, L., & Sangalli, L. M. (2024). Sign-flip inference for spatial regression with differential regularisation. *Stat*, *13*(3), e711. Retrieved from `https://onlinelibrary.wiley.com/doi/abs/10.1002/sta4.711` doi: 10.1002/sta4.711

Chaudhuri, S., Juan, P., Saurina, L. S., Varga, D., & Saez, M. (2023). Modeling spatial dependencies of natural hazards in coastal regions: a nonstationary approach with barriers. *Stochastic Environmental Research and Risk Assessment*. Retrieved from `https://doi.org/10.1007/s00477-023-02519-9` doi: 10.1007/s00477-023-02519-9

Chen, W., Li, Y., Reich, B. J., & Sun, Y. (2022). *DeepKriging: Spatially Dependent Deep Neural Networks for Spatial Prediction.*

Cox, D. D. (1984). Multivariate Smoothing Spline Functions. *SIAM Journal on Numerical Analysis*, *21*(4), 789–813. Retrieved from `http://www.jstor.org/stable/2157009`

Craven, P., & Wahba, G. (1978). Smoothing noisy data with spline functions. *Numerische Mathematik*, *31*(4), 377–403. Retrieved from `https://doi.org/10.1007/BF01404567` doi: 10.1007/BF01404567

Cressie, N., & Wikle, C. K. (2011). *Statistics for Spatio-Temporal Data*. Wiley.

Davis, N., Badger, J., Hahmann, A. N., Hansen, B. O., Olsen, B. T., Mortensen, N. G., … Lacave, O. (2019). *Global Wind Atlas v3*. Retrieved from `https://data.dtu.dk/articles/dataset/Global_Wind_Atlas_v3/9420803` Wind atlas available at `https://globalwindatlas.info/en/area/Switzerland`. Accessed: 2023-07-26. doi: 10.11583/DTU.9420803.v1

Diggle, P., & Ribeiro, P. J. (2007). *Model-based Geostatistics*. Springer New York.

Dubois, G., Malczewski, J., & De Cort, M. J. M. R. (2003). *Mapping Radioactivity in the Environment: Spatial Interpolation Comparison 97*. Office for Official Publications of the European Communities. Retrieved from `https://publications.jrc.ec.europa.eu/repository/handle/JRC24971` Switzerland rainfall data available at `ftp://ftp.geog.uwo.ca/SIC97/intro/alldata.dat`. Accessed: 2022-02-17.

Earth Space Research. (2009). *Ocean Surface Current Analyses-Real time (OSCAR)*. `https://podaac.jpl.nasa.gov/dataset/OSCAR_L4_OC_third-deg`. Accessed: 2022-08-20.

Ettinger, B., Perotto, S., & Sangalli, L. M. (2016). Spatial regression models over two-dimensional manifolds. *Biometrika*, *103*(1), 71–88. Retrieved from `https://doi.org/10.1093/biomet/asv069` doi: 10.1093/biomet/asv069

Eubank, R. L. (1999). *Nonparametric Regression and Spline Smoothing*. CRC Press. doi: 10.1201/9781482273144

Ferraccioli, F., Arnone, E., Finos, L., Ramsay, J. O., & Sangalli, L. M. (2021). Nonparametric Density Estimation Over Complicated Domains. *Journal of the Royal Statistical Society Series B: Statistical Methodology*, *83*(2), 346–368. Retrieved from `https://doi.org/10.1111/rssb.12415` doi: 10.1111/rssb.12415

Ferraccioli, F., Sangalli, L. M., & Finos, L. (2022). Some first inferential tools for spatial regression with differential regularization. *Journal of Multivariate Analysis*, *189*, 104866. Retrieved from `https://www.sciencedirect.com/science/article/pii/S0047259X21001445` doi: 10.1016/j.jmva.2021.104866

Ferraccioli, F., Sangalli, L. M., & Finos, L. (2023). Nonparametric tests for semiparametric regression models. *TEST*, *32*(3), 1106-1130. Retrieved from `https://doi.org/10.1007/s11749-023-00868-9` doi: 10.1007/s11749-023-00868-9

Fuglstad, G.-A., Lindgren, F., Simpson, D., & Rue, H. (2015). Exploring a new class of non-stationary spatial gaussian random fields with varying local anisotropy. *Statistica Sinica*, *25*(1), 115–133. Retrieved 2023-11-16, from `http://www.jstor.org/stable/24311007` doi: 10.5705/ss.2013.106w

Fuglstad, G.-A., Simpson, D., Lindgren, F., & Rue, H. (2015). Does non-stationary spatial data always require non-stationary random fields? *Spatial Statistics*, *14*. doi: 10.1016/j.spasta.2015.10.001

Grieshop, N., & Wikle, C. K. (2023). Data-driven modeling of wildfire spread with stochastic cellular automata and latent spatio-temporal dynamics. *Spatial Statistics*, 100794. Retrieved from `https://www.sciencedirect.com/science/article/pii/S2211675323000696` doi: 10.1016/j.spasta.2023.100794

Hefley, T. J., Hooten, M. B., Russell, R. E., Walsh, D. P., & Powell, J. A. (2017). When mechanism matters: Bayesian forecasting using models of ecological diffusion. *Ecology Letters*, *20*(5), 640–650. Retrieved from `https://onlinelibrary.wiley.com/doi/abs/10.1111/ele.12763` doi: 10.1111/ele.12763

JPL MUR MEaSUREs Project. (2015). *GHRSST Level 4 MUR Global Foundation Sea Surface Temperature Analysis. Ver. 4.1. PO.DAAC, CA, USA.* `https://podaac.jpl.nasa.gov/dataset/MUR-JPL-L4-GLOB-v4.1`. Accessed: 2022-08-20.

Jr, P. J. R., & Diggle, P. J. (2001). geoR: a package for geostatistical analysis. *R-NEWS*, *1*(2), 14–18. Retrieved from `http://CRAN.R-project.org/doc/Rnews/` ISSN 1609-3631.

Krainski, E., Gómez Rubio, V., Bakka, H., Lenzi, A., Castro-Camilo, D., Simpson, D., … Rue, H. (2018). *Advanced Spatial Modeling with Stochastic Partial Differential Equations Using R and INLA*. CRC Press. doi: 10.1201/9780429031892

Kuhnert, P. (2014). Physical-statistical modelling. *Environmetrics*, *25*(4), 201–202. Retrieved from `https://onlinelibrary.wiley.com/doi/abs/10.1002/env.2276` doi: 10.1002/env.2276

Lai, M.-J., & Schumaker, L. L. (2007). *Spline Functions on Triangulations*. Cambridge University Press. doi: 10.1017/CBO9780511721588

Lai, M.-J., & Wang, L. (2013). Bivariate Penalized Splines for Regression. *Statistica Sinica*, *23*, 1399-–1417. doi: 10.5705/ss.2010.278

Lenzi, A., Bessac, J., Rudi, J., & Stein, M. L. (2023). Neural networks for parameter estimation in intractable models. *Computational statistics & Data Analysis*, *185*. Publisher Copyright: © 2023 Elsevier B.V.. doi: 10.1016/j.csda.2023.107762

Lindgren, F., Bolin, D., & Rue, H. (2022). The SPDE approach for Gaussian and non-Gaussian fields: 10 years and still running. *Spatial Statistics*, *50*, 100599. Retrieved from `https://www.sciencedirect.com/science/article/pii/S2211675322000057` Special Issue: The Impact of Spatial Statistics. doi: 10.1016/j.spasta.2022.100599

Lindgren, F., Rue, H., & Lindström, J. (2011). An explicit link between Gaussian fields and Gaussian Markov random fields: the stochastic partial differential equation approach. *Journal of the Royal Statistical Society: Series B (Statistical Methodology)*, *73*(4), 423–498. Retrieved from `https://rss.onlinelibrary.wiley.com/doi/abs/10.1111/j.1467-9868.2011.00777.x` doi: 10.1111/j.1467-9868.2011.00777.x

Marra, G., Miller, D., & Zanin, L. (2012). Modelling the Spatiotemporal Distribution of the Incidence of Resident Foreign Population. *Statistica Neerlandica*, *66*, 133–160. doi: 10.1111/j.1467-9574.2011.00500.x

Martins, T. G., Simpson, D., Lindgren, F., & Rue, H. (2013). Bayesian computing with INLA: New features. *Computational Statistics & Data Analysis*, *67*, 68–83. Retrieved from `https://www.sciencedirect.com/science/article/pii/S0167947313001552` doi: 10.1016/j.csda.2013.04.014

Menicali, L., Richter, D. H., & Castruccio, S. (2023). *Physics-Informed Priors with Application to Boundary Layer Velocity.*

National Data Buoy Center. (2023). *Standard Meteorological Data by Station.* `https://www.ndbc.noaa.gov`. National Oceanic and Atmospheric Administration. Accessed: 2020-04-10.

Pebesma, E. J. (2004). Multivariable geostatistics in S: the gstat package. *Computers & Geosciences*, *30*(7), 683–691. Retrieved from `https://www.sciencedirect.com/science/article/pii/S0098300404000676` doi: 10.1016/j.cageo.2004.03.012

Peli, R., Menafoglio, A., Cervino, M., Dovera, L., & Secchi, P. (2022). Physics-based Residual Kriging for dynamically evolving functional random fields. *Stochastic Environmental Research and Risk Assessment*, *36*, 3063–3080. Retrieved from `https://doi.org/10.1007/s00477-022-02180-8` doi: 10.1007/s00477-022-02180-8

Ramsay, J. O., Hooker, G., Campbell, D., & Cao, J. (2007). Parameter estimation for differential equations: A generalized smoothing approach. *Journal of the Royal Statistical Society: Series B (Statistical Methodology)*, *69*(5), 741–796. Retrieved from `https://rss.onlinelibrary.wiley.com/doi/abs/10.1111/j.1467-9868.2007.00610.x` doi:

10.1111/j.1467-9868.2007.00610.x

Ramsay, T. (2002). Spline smoothing over difficult regions. *Journal of the Royal Statistical Society. Series B: Statistical Methodology*, *64*(2), 307–319. Retrieved from `https://www.scopus.com/inward/record.uri?eid=2-s2.0-0036013002&doi=10.1111%2f1467-9868.00339&partnerID=40&md5=8933aa657dd0468917474878c9f5cbb2` doi: 10.1111/1467-9868.00339

Richardson, R. A. (2017). Sparsity in nonlinear dynamic spatiotemporal models using implied advection. *Environmetrics*, *28*(6), e2456. Retrieved from `https://onlinelibrary.wiley.com/doi/abs/10.1002/env.2456` e2456 env.2456. doi: 10.1002/env.2456

Rue, H., Martino, S., & Chopin, N. (2009). Approximate Bayesian inference for latent Gaussian models by using integrated nested Laplace approximations. *Journal of the Royal Statistical Society: Series B (Statistical Methodology)*, *71*(2), 319–392. Retrieved from `https://rss.onlinelibrary.wiley.com/doi/abs/10.1111/j.1467-9868.2008.00700.x` doi: 10.1111/j.1467-9868.2008.00700.x

Sangalli, L. M. (2021). Spatial Regression With Partial Differential Equation Regularisation. *International Statistical Review*, *89*(3), 505–531. Retrieved from `https://onlinelibrary.wiley.com/doi/abs/10.1111/insr.12444` doi: 10.1111/insr.12444

Sangalli, L. M., Ramsay, J. O., & Ramsay, T. O. (2013). Spatial spline regression models. *Journal of the Royal Statistical Society: Series B (Statistical Methodology)*, *75*(4), 681–703. Retrieved from `https://rss.onlinelibrary.wiley.com/doi/abs/10.1111/rssb.12009` doi: 10.1111/rssb.12009

Schlather, M., Malinowski, A., Menck, P. J., Oesting, M., & Strokorb, K. (2015). Analysis, Simulation and Prediction of Multivariate Random Fields with Package RandomFields. *Journal of Statistical Software*, *63*(8), 1–25. Retrieved from `http://www.jstatsoft.org/v63/i08/` doi: 10.18637/jss.v063.i08

Schlather, M., Malinowski, A., Oesting, M., Boecker, D., Strokorb, K., Engelke, S., … R Core Team (2017). RandomFields: Simulation and Analysis of Random Fields [Computer software manual]. Retrieved from `https://cran.r-project.org/package=RandomFields` R package version 3.1.50.

Scott-Hayward, L. A. S., Mackenzie, M. L., Donovan, C. R., Walker, C. G., & Ashe, E. (2014). Complex Region Spatial Smoother (CReSS). *Journal of Computational and Graphical Statistics*, *23*(2), 340-360. Retrieved from `https://doi.org/10.1080/10618600.2012.762920` doi: 10.1080/10618600.2012.762920

Wahba, G. (1981). Spline Interpolation and Smoothing on the Sphere. *SIAM Journal on Scientific and Statistical Computing*, *2*(1), 5–16. Retrieved from 10.1137/0902002 doi: 10.1137/0902002

Wahba, G. (1990). *Spline Models for Observational Data*. Society for Industrial and Applied Mathematics. Retrieved from `https://epubs.siam.org/doi/abs/10.1137/1.9781611970128` doi: 10.1137/1.9781611970128

Wang, H., & Ranalli, M. G. (2007). Low-Rank Smoothing Splines on Complicated Domains. *Biometrics*, *63*(1), 209–217. Retrieved from `https://onlinelibrary.wiley.com/doi/abs/10.1111/j.1541-0420.2006.00674.x` doi: 10.1111/j.1541-0420.2006.00674.x

Wang, L., Wang, G., Lai, M.-J., & Gao, L. (2020). Efficient estimation of partially linear models for data on complicated domains by bivariate penalized splines over triangulations. *Statistica Sinica*, *30*(1), 347–369.

Whittle, P. (1954). On stationary processes in the plane. *Biometrika*, *41*(3-4), 434–449. Retrieved from `https://doi.org/10.1093/biomet/41.3-4.434` doi: 10.1093/biomet/41.3-4.434

Wikle, C. K. (2003). Hierarchical Bayesian Models for Predicting the Spread of Ecological Processes. *Ecology*, *84*(6), 1382–1394. Retrieved from `http://www.jstor.org/stable/3107956`

Wikle, C. K., & Hooten, M. (2010). A general science-based framework for dynamical spatio-temporal models. *TEST*, *19*, 417–451. doi: 10.1007/s11749-010-0209-z

Wikle, C. K., & Zammit-Mangion, A. (2023). Statistical Deep Learning for Spatial and Spatiotemporal Data. *Annual Review of Statistics and Its Application*, *10*(1), 247–270. Retrieved from `https://doi.org/10.1146/annurev-statistics-033021-112628` doi: 10.1146/annurev-statistics-033021-112628

Wilhelm, M., & Sangalli, L. M. (2016). Generalized spatial regression with differential regularization. *Journal of Statistical Computation and Simulation*, *86*(13), 2497–2518. Retrieved from `https://doi.org/10.1080/00949655.2016.1182532` doi: 10.1080/00949655.2016.1182532

Wood, S. N., Bravington, M. V., & Hedley, S. L. (2008). Soap film smoothing. *Journal of the Royal Statistical Society: Series B (Statistical Methodology)*, *70*(5), 931–955. Retrieved from `https://rss.onlinelibrary.wiley.com/doi/abs/10.1111/j.1467-9868.2008.00665.x` doi: 10.1111/j.1467-9868.2008.00665.x

Xun, X., Cao, J., Mallick, B., Maity, A., & Carroll, R. J. (2013). Parameter Estimation of Partial Differential Equation Models. *Journal of the American Statistical Association*, *108*(503), 1009–1020. Retrieved 2023-09-07, from `http://www.jstor.org/stable/24246881`

Yu, S., Wang, G., Wang, L., Liu, C., & Yang, L. (2019). Estimation and inference for generalized geoadditive models. *Journal of the American Statistical Association*.

Zammit-Mangion, A., & Wikle, C. K. (2020). Deep integro-difference equation models for spatio-temporal forecasting. *Spatial Statistics*, *37*, 100408. Retrieved from `https://www.sciencedirect.com/science/article/pii/S2211675320300026` Frontiers in Spatial and Spatio-temporal Research. doi: 10.1016/j.spasta.2020.100408

SUPPORTING INFORMATION

7.1 | Definition of finite element matrices

Let $\boldsymbol{\xi}_1, ..., \boldsymbol{\xi}_k$ be the mesh nodes. Let $\boldsymbol{\psi} = (\psi_1, ..., \psi_k)^\top$ be the vector collecting the k finite element bases, that are locally-supported piecewise polynomial functions defined over the domain $\mathcal{D}$ and such that, for $h = 1, ..., k$,

$$\psi_h(\mathbf{p}) = \begin{cases} 1 & \text{if } \mathbf{p} = \boldsymbol{\xi}_h \\ 0 & \text{if } \mathbf{p} = \boldsymbol{\xi}_{\tilde{h}} \quad \forall \tilde{h} \neq h. \end{cases}$$

Define the $n \times k$ matrix Ψ that stores the evaluations of every finite element basis function at the locations $\mathbf{p}_1, ..., \mathbf{p}_n$, i.e., $\{\Psi\}_{i,h} = \psi_h(\mathbf{p}_i)$, for $i = 1, ..., n$ and $h = 1, ..., k$. Define the $k \times k$ matrices

$$R_0 = \int_{\mathcal{D}} \boldsymbol{\psi}\boldsymbol{\psi}^\top d\mathbf{p} \qquad \text{and} \qquad R_1 = \int_{\mathcal{D}} \nabla\boldsymbol{\psi}^\top K\nabla\boldsymbol{\psi} + \nabla\boldsymbol{\psi}^\top \mathbf{b}\boldsymbol{\psi}^\top + c\boldsymbol{\psi}\boldsymbol{\psi}^\top d\mathbf{p}.$$

The mixed finite element approach detailed in Azzimonti et al. (2014, 2015) leads a finite element discretization of the penalization term represented by the matrix $P = R_1^\top R_0^{-1} R_1$.

7.2 | Properties of the estimators

From the expression of the estimators provided in Equation (2), it is straightforward to derive the following first and second moments of the estimators:

$$\mathbb{E}[\hat{\boldsymbol{\beta}}] = \boldsymbol{\beta} + \left(X^\top \Lambda X\right)^{-1} X^\top \Lambda \Psi \mathbf{f}$$

$$Var(\hat{\boldsymbol{\beta}}) = \sigma^2 \left(X^\top \Lambda X\right)^{-1} X^\top \Lambda\Lambda^\top X \left(X^\top \Lambda X\right)^{-1}$$

$$\mathbb{E}[\hat{f}(\mathbf{p})] = \boldsymbol{\psi}(\mathbf{p})^\top \left(\frac{1-\rho}{n}\Psi^\top Q\Psi + \frac{\rho}{|\mathcal{D}|}P\right)^{-1} \frac{1-\rho}{n}\Psi^\top Q\Psi\mathbf{f}$$

$$Var(\hat{f}(\mathbf{p})) = \sigma^2 \boldsymbol{\psi}(\mathbf{p})^\top \left(\frac{1-\rho}{n}\Psi^\top Q\Psi + \frac{\rho}{|\mathcal{D}|}P\right)^{-1} \frac{1-\rho}{n}\Psi^\top Q\Psi\frac{1-\rho}{n} \left(\frac{1-\rho}{n}\Psi^\top Q\Psi + \frac{\rho}{|\mathcal{D}|}P\right)^{-1} \boldsymbol{\psi}(\mathbf{p})$$

$$Cov(\hat{f}(\mathbf{p}), \hat{f}(\tilde{\mathbf{p}})) = \sigma^2 \boldsymbol{\psi}(\mathbf{p})^\top \left(\frac{1-\rho}{n}\Psi^\top Q\Psi + \frac{\rho}{|\mathcal{D}|}P\right)^{-1} \frac{1-\rho}{n}\Psi^\top Q\Psi\frac{1-\rho}{n} \left(\frac{1-\rho}{n}\Psi^\top Q\Psi + \frac{\rho}{|\mathcal{D}|}P\right)^{-1} \boldsymbol{\psi}(\tilde{\mathbf{p}}).$$

Moreover, thanks to the asymptotic normality of the estimators, proven, e.g., in Ferraccioli et al. (2022, 2023) and Arnone, Negri, et al. (2023), it is possible to compute confidence intervals for $\boldsymbol{\beta}$ and f, and prediction intervals for new observations. See also Arnone, Sangalli, and Vicini (2023) for the generalization to space-time settings. More advanced inferential tools, based on innovative resampling strategies, are discussed in Cavazzutti et al. (2024); Ferraccioli et al. (2023) and Ferraccioli et al. (2022).

MOX Technical Reports, last issues

Dipartimento di Matematica

Politecnico di Milano, Via Bonardi 9 - 20133 Milano (Italy)

86/2024 Franco, N.R.; Fraulin, D.; Manzoni, A.; Zunino, P.
On the latent dimension of deep autoencoders for reduced order modeling of PDEs parametrized by random fields

89/2024 Tomasetto, M.; Arnone, E.; Sangalli, L.M.
Modeling anisotropy and non-stationarity through physics-informed spatial regression

88/2024 Regazzoni, F.; Poggesi, C.; Ferrantini, C.
Elucidating the cellular determinants of the end-systolic pressure-volume relationship of the heart via computational modelling

85/2024 Brivio, S.; Franco, Nicola R.; Fresca, S.; Manzoni, A.
Error estimates for POD-DL-ROMs: a deep learning framework for reduced order modeling of nonlinear parametrized PDEs enhanced by proper orthogonal decomposition

83/2024 Conti, P.; Guo, M.; Manzoni, A.; Frangi, A.; Brunton, S. L.; Kutz, J.N.
Multi-fidelity reduced-order surrogate modelling

82/2024 Rosafalco, L.; Conti, P.; Manzoni, A.; Mariani, S.; Frangi, A.
EKF-SINDy: Empowering the extended Kalman filter with sparse identification of nonlinear dynamics

80/2024 Crippa, B.; Scotti, A.; Villa, A
Numerical Solution of linear drift-diffusion and pure drift equations on one-dimensional graphs

79/2024 Baioni, P.J.; Benacchio, T.; Capone, L.; de Falco, C.
Portable, Massively Parallel Implementation of a Material Point Method for Compressible Flows

78/2024 Ziarelli, G.; Pagani, S.; Parolini, N.; Regazzoni, F.; Verani, M.
A model learning framework for inferring the dynamics of transmission rate depending on exogenous variables for epidemic forecasts

77/2024 Piersanti, R.; Bradley, R.; Ali, S.Y.; Quarteroni A.; Dede', L; Trayanova, N.A.
Defining myocardial fiber bundle architecture in atrial digital twins